

Climatology of Clear-Air Turbulence in Upper Troposphere and Lower Stratosphere in the Northern Hemisphere using ERA5 reanalysis data

Juheon Lee¹, Jung-Hoon Kim¹, Robert D. Sharman², Joowan Kim³, and Seok-Woo Son¹

¹Seoul National University

²National Center for Atmospheric Research (UCAR)

³Kongju National University

November 23, 2022

Abstract

Spatial and temporal distributions of Clear-Air Turbulence (CAT) in the Northern Hemisphere were investigated using 41 years (1979 – 2019) of the European Centre for Medium-range Weather Forecast Reanalysis version 5 (ERA5) data. We used two groups of CAT diagnostics to determine occurrence frequencies: 1) commonly used empirical turbulence indices (TI1, TI2, and TI3) and their components [vertical wind shear (VWS), deformation, divergence, and divergence tendency], and 2) theoretical instability indicators Richardson number (Ri), potential vorticity (PV), and Brunt-Väisälä frequency. The empirical indices showed high frequencies of MOG-level CAT potential over the East Asian, Eastern Pacific, and Northwest Atlantic regions in winter. Over East Asia, the entrance region of the strong upper-level jets, showed the highest frequencies in TI1, TI2, and TI3 mainly due to strong VWS. The Eastern Pacific and Northwestern Atlantic areas near the exit region of the jet had relatively high frequencies of these and also Ri. PV frequency was high on the southern side of the jet primarily due to negative relative vorticity. Long-term increasing trends of MOG-level CAT potential also appeared in those three regions mainly due to the warming in lower latitudes. The most significant increasing trend was found over East Asia, due to the strengthening of the East Asian jet and VWS due to the strong meridional temperature gradients in the mid-troposphere induced by warming in the tropics and cooling in eastern Eurasia. These trends over East Asia are expected to be of importance to efficient aviation operations across the northwestern Pacific Ocean.

Climatology of Clear-Air Turbulence in Upper Troposphere and Lower Stratosphere in the Northern Hemisphere using ERA5 reanalysis data

Juheon Lee¹, Jung-Hoon Kim^{1*}, R. D. Sharman², Joowan Kim³, and Seok-Woo Son¹

¹ School of Earth and Environmental Sciences, Seoul National University, Seoul, South Korea.

² National Center for Atmospheric Research, Boulder, CO, USA.

³ Department of Atmospheric Science, Gongju National University, Gongju, South Korea.

Corresponding author: Jung-Hoon Kim (jhkim99@snu.ac.kr)

† Prof. Jung-Hoon Kim, PhD, School of Earth and Environmental Sciences (SEES), Seoul, South Korea, 08826.

Key Points:

- Spatial and temporal distributions of Clear-Air Turbulence (CAT) indices for 41 years in NH are derived using the highest resolution of reanalysis data
- CAT potentials are high in three regions: the East Asian, Eastern Pacific, and Northwest Atlantic regions due to upper-level jets.
- The strongest increasing trend is in East Asia due to warming in tropics and cooling over the Eurasian continent, which may have a high impact on transpacific flights.

Abstract

The spatial and temporal distributions of Clear-Air Turbulence (CAT) in the Northern Hemisphere were investigated using 41 years (1979 – 2019) of the European Centre for Medium-range Weather Forecast Reanalysis version 5 (ERA5) data. We used two groups of CAT diagnostics to determine occurrence frequencies: 1) commonly used empirical turbulence indices (TI1, TI2, and TI3) and their components [vertical wind shear (VWS), deformation, divergence, and divergence tendency], and 2) theoretical instability indicators Richardson number (Ri), potential vorticity (PV), and Brunt-Väisälä frequency. The empirical indices showed high frequencies of MOG-level CAT potential over the East Asian, Eastern Pacific, and Northwest Atlantic regions in winter. Over East Asia, the entrance region of the strong upper-level jets, showed the highest frequencies in TI1, TI2, and TI3 mainly due to strong VWS. The Eastern Pacific and Northwestern Atlantic areas near the exit region of the jet had relatively high frequencies of these and also Ri. PV frequency was high on the southern side of the jet primarily due to negative relative vorticity. Long-term increasing trends of MOG-level CAT potential also appeared in those three regions mainly due to the warming in lower latitudes. The most significant increasing trend was found over East Asia, due to the strengthening of the East Asian jet and VWS due to the strong meridional temperature gradients in the mid-troposphere induced by warming in the tropics and cooling in eastern Eurasia. These trends over East Asia are expected to be of importance to efficient aviation operations across the northwestern Pacific Ocean.

1 Introduction

The jet stream associated vertical wind shears are strongest in middle latitudes in the upper troposphere ($z = 8\text{--}12$ km), and their existence is largely explained by the meridional temperature gradient between tropics and polar regions via the thermal wind relation (e.g., Holton, 1992; Lee et al., 2019). Jets are closely associated with dynamic weather phenomena such as storm tracks and cyclogenesis. However, they are also responsible for aviation weather hazards including upper-level turbulence encountered by cruising aircraft in the upper troposphere and lower stratosphere (UTLS) (e.g., Kim et al., 2016; Kim & Chun, 2011; Sharman et al., 2012). These turbulence encounters are commonly referred to as Clear-Air Turbulence (CAT) which often occurs in the vicinity of the jet stream without visually detectable convective clouds (e.g., Kim et al., 2011, 2018; Lester, 1994; Sharman et al., 2006). CAT may be generated by a variety of mechanisms, including but not limited to shear instability, frontogenesis near upper-level jet/frontal systems (Dutton & Panofsky, 1970; Ellrod & Knapp, 1992), and emissions of inertia gravity waves via geostrophic adjustments at the exit region of jet streams (e.g., Ellrod & Knox, 2010; Koch et al., 2005; Lane et al., 2004; Zhang, 2004). Inertial instability developed in anticyclonic shear and curvature flows may also be an important source for CAT (e.g., Kim et al., 2014; Knox, 1997).

Moderate-or-greater (MOG) intensity CAT can cause structural damage to aircraft and serious physical injuries to crews or passengers. These problems in turn lead to economic loss and flight delays (Kim et al., 2016, 2018; Sharman et al., 2006; Sharman & Pearson, 2017; Wolff & Sharman, 2008). Therefore, long-haul flight routes across the oceans and continents need to be planned to minimize possible CAT encounters for efficient and safe flights. However, CAT forecasting is challenging due to its isolated nature and small-scale motion (turbulent eddies of

~10-1000 m in horizontal scale) compared to current numerical weather prediction (NWP) model resolutions (e.g., Lester, 1994; Sharman et al., 2006, 2014; Sharman & Pearson, 2017). However, CAT can be diagnosed with some reliability from NWP models using empirical turbulence indices and theoretical instability indicators under the assumption that the turbulence is supposed to be originate at resolved scales and cascades down to smaller eddies that may affect aircraft (e.g., Cho & Lindborg, 2001; Kim et al., 2011, 2018; Kim & Chun, 2010; Sharman et al., 2006, 2014).

As the meridional temperature gradients have increased in some regions mainly due to global warming, jet streams have correspondingly modulated over the past decades (e.g., Lee et al., 2019; Lv et al., 2021). Consequently, the potential of CAT is expected to increase over some regions. Jaeger and Sprenger (2007) showed spatial distributions and trends of four CAT diagnostics in the UTLS NH using the European Centre for Medium range Weather Forecast (ECMWF) Re-Analysis 40 (ERA40) data with T159 (~90 km) horizontal resolution for 44 years (1958-2001). They identified a 40-90% frequency increase of CAT according to the diagnostics used over the North Atlantic, United States and European sectors. Kim et al. (2016) also showed variations in CAT potential along the flight routes during two distinct North Atlantic Oscillation (NAO) patterns. Lee et al. (2019) analyzed temperature and vertical wind shear (VWS) trends in the North Atlantic region from 1979 to 2017 using three reanalysis datasets from the ECMWF, National Centers for Environmental Prediction/National Center for Atmospheric Research, and Japanese Meteorological Agency. They found an intensification of VWS and therefore CAT potential of about 11-17% for the study period. Similar trends are found on several future projections of climate model data, showing that the occurrence frequency of CAT will be stronger along with the modified jet stream (Storer et al., 2017; Williams, 2017; Williams & Joshi, 2013). Therefore, it becomes important to understand the details of CAT climatology in the NH during the era of climate change.

This study aims to analyze historical patterns and trends of CAT in the recent four decades (1979 – 2019) using the highest resolution reanalysis data available and extends the findings of previous studies in three ways. First, we calculated a total of ten empirical and theoretical diagnostics to identify various generation mechanisms of CAT near upper-level jets and their contributions to CAT climatology, whereas previous NH CAT climatology studies used relatively fewer diagnostics. Second, we examined the long-term trends of CAT diagnostics over the entire NH, while the previous studies investigated the trends of CAT potential only in specific areas. Finally, we focus on the East Asian region, because this area has the strongest increasing trend of CAT in NH in response to climate change. In section 2, the data and methodology used in this study will be introduced. The result of CAT climatologies and interpretations will be discussed in section 3, followed by a summary and conclusions in Section 4.

2 Data and Methodology

In this study, we used the ECMWF Re-Analysis version 5 (ERA5) data, which has $0.25^\circ \times 0.25^\circ$ horizontal grid spacing over the global domain. At the moment, the ERA5 has the finest resolution among existing global reanalysis datasets. The higher horizontal resolution facilitates a clear identification of CAT features in local areas. To examine CAT potential, we used 6-hourly data (00, 06, 12, and 18 UTC) from 41-year record of ERA5 from January 1979 to December 2019.

We calculated the CAT potential in the UTLS using twelve vertical layers between 100 and 500 hPa levels (100, 125, 175, 200, 225, 250, 300, 350, 400, 450, and 500 hPa), which has sufficient vertical resolution to calculate variabilities associated with vertical shear and upper-level jet streams near the tropopause and typical cruising levels (e.g. 250 hPa) (Kim et al., 2020).

We used two groups (empirical indices and theoretical instability indicators) of CAT diagnostics in this study. The empirical diagnostics used are the Turbulence Index versions 1, 2, and 3 (TI1, TI2, and TI3) and their components [vertical wind shear (VWS), deformation (DEF), -divergence (-DIV), and divergence trend (DVT)]. TI1 is a product of VWS and DEF, which indicates CAT caused by shear instability and frontogenesis (Ellrod & Knapp, 1992). Shear instability diagnosed by VWS is strong above and below the jet stream (Kim & Chun, 2010). Frontogenesis caused by DEF appears on the cyclonic shear side of the jet stream due to strong meridional temperature gradients, which increases VWS in accordance with thermal wind relationship (Ellrod & Knapp, 1992). Therefore, the TI1 index has been widely used as one of top diagnostics for CAT forecasting at several weather prediction centers (e.g., Kim et al., 2018). TI2 additionally considers convergent flow (-DIV) related to development of upper-level frontal zones, which in turn strengthens VWS (Ellrod, 1985). Finally, TI3 replaces the divergence term in TI2 with divergence tendency (DVT) that may contribute to the generation of inertia gravity waves via geostrophic adjustment processes or spontaneous imbalance (e.g., Ellrod & Knox, 2010; Knox et al., 2008). TI1, TI2 and TI3 are calculated by the following equations.

$$TI1 = VWS \times DEF = \left(\left(\frac{\partial u}{\partial z} \right)^2 + \left(\frac{\partial v}{\partial z} \right)^2 \right)^{1/2} \left(\left(\frac{\partial u}{\partial x} - \frac{\partial v}{\partial y} \right)^2 + \left(\frac{\partial v}{\partial x} + \frac{\partial u}{\partial y} \right)^2 \right)^{1/2} \quad \dots(1)$$

$$TI2 = VWS \times (DEF - DIV) \\ = \left(\left(\frac{\partial u}{\partial z} \right)^2 + \left(\frac{\partial v}{\partial z} \right)^2 \right)^{1/2} \left[\left(\left(\frac{\partial u}{\partial x} - \frac{\partial v}{\partial y} \right)^2 + \left(\frac{\partial v}{\partial x} + \frac{\partial u}{\partial y} \right)^2 \right)^{1/2} - \left(\frac{\partial u}{\partial x} + \frac{\partial v}{\partial y} \right) \right] \quad \dots(2)$$

$$TI3 = TI1 + DVT, \quad DVT = C \left| \left(\frac{\partial u}{\partial x} + \frac{\partial v}{\partial y} \right)_{t_2} - \left(\frac{\partial u}{\partial x} + \frac{\partial v}{\partial y} \right)_{t_1} \right| \quad \dots(3)$$

where u is zonal wind speed and v is meridional wind speed. DVT was calculated by using the difference between the present data (t_2) and the previous data six hours earlier (t_1). The empirical constant value C is a scaling parameter to adjust the magnitude of DVT to be of the same magnitude as TI1, which was estimated by probability density functions following the method outlined in previous studies (Lee et al., 2020). From the PDFs it was found that the peaks appeared around 1.82×10^{-7} and 2.37×10^{-5} for TI1 and DVT, respectively. Therefore, we set the scaling parameter of C to be 0.01, so that the DVT has the similar magnitude as TI1 (e.g., Lee et al., 2020).

In addition to the empirical diagnostics TI1, TI2, and TI3, we also considered three “theoretical” instability diagnostics: the Brunt-Väisälä frequency (N^2), Richardson number (Ri), and potential vorticity (PV), which are directly related to convective, Kelvin-Helmholtz, and inertial instabilities, respectively. These diagnostics are termed “theoretical” here since they are based on various simplified instability theories. Convective instability is generated when N^2 becomes negative. Statically unstable flows are associated with convective overturning, which can

lead to CAT (e.g., Jaeger & Sprenger, 2007). Ri less than some small number indicates Kelvin-Helmholtz instability developed when VWS is large and/or N^2 is small. We set the threshold of Ri to $0 < Ri < 1$ in this study to separate Kelvin-Helmholtz instability from convective instability when $N^2 < 0$ (e.g., Abarbanel et al., 1984; Jaeger & Sprenger, 2007; Kim & Chun, 2010, 2012). The condition $PV < 0$ is used here primarily to identify regions of inertial instability (e.g., Kim et al. 2014; Knox & Harvey, 2005; Sato & Dunkerton, 2002; Trier & Sharman, 2016) which may be favorable for the generation of CAT. Inertial instability is primarily generated by negative relative vorticity in strong anticyclonic shear and curvature flows in the NH (e.g., Holton, 1992; Jaeger & Sprenger, 2007; Thompson et al., 2018). However, as with the Ri, PV can be negative when the absolute vorticity is positive and $N^2 < 0$ as well. The theoretical indicator equations are as follows.

$$N^2 = \frac{g}{\theta} \frac{\partial \theta}{\partial z} \quad \dots(4)$$

$$Ri = \frac{N^2}{VWS^2} \quad \dots(5)$$

$$PV = \frac{1}{\rho} (\zeta + f) \frac{\partial \theta}{\partial z} \quad \dots(6)$$

where θ , ζ , ρ , and f represent the potential temperature, the relative vorticity, the air density, and the Coriolis parameter, respectively.

To examine the spatial and temporal distributions of MOG-level CAT, we need to establish thresholds of each CAT index. While thresholds of theoretical instability indices are established according to dynamical considerations, the MOG thresholds for the empirical indices were determined by calculating a top percentile of the probability density function (PDF) of each diagnostic from the ERA5 data, as was done in Williams (2017). Kim and Chun (2011) and Lee and Chun (2015) found that 3-4 % of CAT incidents occurring over South Korea and East Asia where the strongest jet streams exists were in the MOG category. Wolff and Sharman (2008) and Sharman et al. (2014) estimated climatological upper-level MOG turbulence frequency at 1-2% based on pilot reports and in situ turbulence observation data from commercial aircraft in United States, respectively. Williams (2017) set the probability of MOG-level CAT to the top 0.4 percentile of the calculated CAT diagnostics. However, the in situ aircraft-based studies only consider turbulence encountered by cruising aircraft and those can be underestimated by avoiding already forecasted areas (Colson, 1963; Sharman et al., 2014). Therefore, given that this study focused on the frequency of CAT in the UTLS near upper-level jet streams, we choose the 95th percentile value as the thresholds of each CAT index for MOG-level CAT (e.g., Lee et al., 2020).

Figure 1 shows the probability density functions (PDFs) of the empirical CAT diagnostics (VWS, DEF, DIV, DVT, TI1, TI2, and TI3) for summer (JJA; red histograms) and winter (DJF; blue histograms) during the research period (41 years: 1979 – 2019). To incorporate two different seasons with one representative threshold for each diagnostic, the 95% values were computed from the sum of summer and winter PDFs for each index, which is indicated by black dashed vertical lines in Figure 1. Here, all PDFs were calculated at a typical cruising altitude of 250 hPa for commercial aircraft in the midlatitude regions (20-60° N) where the climatological jet stream is located. Table 1 shows the determined thresholds of each index.

189

CAT Index	MOG Threshold	Unit
VWS	$> 1.03 \times 10^{-2}$	s^{-1}
DEF	$> 1.29 \times 10^{-4}$	s^{-1}
-DIV	$> 5.15 \times 10^{-5}$	s^{-1}
DVT	$> 7.18 \times 10^{-5}$	s^{-1}
TI1	$> 9.07 \times 10^{-7}$	s^{-1}
TI2	$> 1.03 \times 10^{-6}$	s^{-1}
TI3	$> 1.39 \times 10^{-6}$	s^{-1}
N^2	< 0	s^{-2}
PV	< 0	1 PVU
Ri	$0 < \text{Ri} < 1$	dimensionless

190 **Table 1.** Thresholds from the calculated 95th percentile values of the PDFs for the empirical CAT
 191 indices at 250 hPa in the 20-60° N for 41 years (1979 – 2019), and thresholds for theoretical
 192 instability indicators with their units.

193

194 3 Results

195 3.1 Case Study

196 A case study was performed to ensure whether the determined threshold of each empirical
 197 index properly captures the occurrence of MOG-level CAT. At 1010 UTC and 1125 UTC 11
 198 October 2012, two flights from Incheon, South Korea to San Francisco and Seattle, respectively,
 199 encountered MOG-level CAT at about 11 km altitude (~225 hPa) when crossing over the
 200 Northwestern Pacific Ocean (Kim et al., 2022). Figure 2a and 2b indicate the evolution of the
 201 large-scale flow associated with the turbulence events with the horizontal wind speed and
 202 geopotential height at 225 hPa at 0600 UTC and 1100 UTC. At 0600 UTC, the jet stream ($> 50 \text{ m}$
 203 s^{-1}) including turbulence spots was located over the Northwestern Pacific Ocean. After five hours
 204 at 1100 UTC, the jet was enhanced with the jet core exceeding 70 m s^{-1} on the western side of the
 205 turbulence regions. This implies that the difference in wind speed from lower levels had increased
 206 around the incident time and consequently the VWS intensified significantly to have much higher

values than the determined threshold ($1.03 \times 10^{-2} \text{ s}^{-1}$) as shown in Fig. 2d and was then main source of the turbulence events.

The turbulence driven by this strong VWS was diagnosed well with both the theoretical instability indicators and the empirical indices (Fig. 2c). First of all, the value of Ri less than one (orange solid contour) was locally located on the eastern side of the turbulence events. Though it did not cover the turbulence spots because of very statically stable conditions in this area ($N^2 > 0$; not shown), the shear instability inducing the MOG-level CAT did exist over the incident region. The empirical indices $TI1$, $TI2$, and $TI3$ also appropriately diagnosed the CAT events by showing high values above the pre-determined thresholds within the incident region. Furthermore, given that their patterns coincided with that of VWS (Fig. 2d), we suppose that the empirical indices diagnosed the turbulence events based on the enhanced VWS (Fig. 2d). Therefore, based on this one case we assume that the determined thresholds from the previous section are reliable enough to identify the regions of MOG-level CAT for developing a CAT climatology in the NH. The slightly different patterns of $TI1$, $TI2$, and $TI3$ were due to high values of the other components (i.e., DEF , $-DIV$, and DVT ; not shown).

3.2 Horizontal Distribution

In this section, we provide horizontal distributions of CAT indices to identify spatial patterns of climatologies of upper-level CAT generation mechanisms in the NH. Figures 3-6 show the frequency distributions of each index for the 41 years (1979 – 2019) at 250 hPa ($\sim 34,000$ ft or 10.4 km) in the NH for winter (DJF) and summer (JJA) based on the determined thresholds (Table 1). Each was calculated as the ratio (%) of the number of values that exceed the thresholds at each grid box in the 6-hourly data during the 41 years, as was done in previous studies (e.g., Jaeger and Sprenger, 2007; Kim and Chun, 2011; Williams, 2017).

Focusing first on winter (Figs. 3 and 4), comparing the average zonal wind speed to the frequency of empirical indices above the 95th percentile threshold, the highest frequencies are generally seen on the northern side of the jet. It is consistent with the results of Jaeger and Sprenger (2007) in which the indicators based on deformation such as $TI1$ were found to be more frequent in cyclonic flows. $TI1$, $TI2$, and $TI3$ showed local maxima over East Asian ($80\text{--}150^\circ\text{E}$, $30\text{--}45^\circ\text{N}$), Eastern Pacific ($170^\circ\text{E}\text{--}130^\circ\text{W}$, $35\text{--}55^\circ\text{N}$), and Northwest Atlantic ($80\text{--}20^\circ\text{W}$, $35\text{--}60^\circ\text{N}$) regions near the entrance and exit of climatological upper-level jets (Fig. 3a, 3b, and 3c). The highest frequencies of $TI1$, $TI2$, and $TI3$ appeared over East Asia (maximum value of $TI1 = 25.84\%$; $TI2 = 27.10\%$; $TI3 = 22.17\%$) and are primarily due to VWS (Fig. 4a) associated with the East Asian jet entrance region. The acceleration of the zonal wind driven by opposite Coriolis torques in the upper and lower sides of ageostrophic secondary circulation at the jet entrance increases the wind speed in the UTLS, which strengthens the local VWS.

Additional local maxima of $TI1$, $TI2$, and $TI3$ were also found over the Eastern Pacific (maximum value of $TI1 = 14.57\%$; $TI2 = 12.45\%$; $TI3 = 16.84\%$) and Northwestern Atlantic (maximum value of $TI1 = 11.84\%$; $TI2 = 10.48\%$; $TI3 = 13.52\%$) located at the exit region of jet stream. These were induced by large DEF , $-DIV$, and DVT in the vicinity of the jet exit as well as VWS. Large-scale deformation at the exit of the jet and convective flows due to storm tracks in

these regions manifested high frequencies of DEF at the exit region of the Pacific and Atlantic jets as shown in Fig. 4b. Large patterns of convergence indicated by -DIV as shown in Fig. 4c are due to decreasing wind speed within the exit region of the jet stream. Maximum patterns of divergence tendency at the exit of the jet stream are shown on Fig. 4d, which of course contributes to higher frequencies of TI3 in these regions compared to TI1 and TI2 by additionally considering CAT generation probably related to inertia gravity waves. Another interesting feature is the locally high frequencies over mountain regions such as Himalaya, Rockies, Alps, and Greenland. These are probably due to mesoscale mountain waves that can be partially resolved by the high resolution ERA5 data and are most apparent in the DEF, DIV, and DVT terms.

On the other hand, the theoretical index Ri correlated with shear instability showed somewhat different patterns from those of empirical indices. Higher frequencies of lowered Ri occurred over the Eastern Pacific and Northwest Atlantic regions, while minimum frequencies appeared over East Asia (Fig. 3e). The results over the Eastern Pacific and North Atlantic are due to the relatively high frequencies of VWS developed at the exit region of the jets (Fig. 4a). Moreover, these regions are areas of nominal storm tracks (Fig. 3d) involving relatively low static stability that contributes to relatively lowered values of positive Ri. (Here, note that magnitude of N^2 frequency is smaller than other indices due to insufficient upper-level vertical layers of ERA5 data. Therefore, we focused on a relative frequency distribution indicating CAT potential by N^2 in the NH, not on an absolute frequency value.) In contrast, East Asia had the least frequency of lowered Ri despite the highest frequency of VWS [maximum value of 35.90% (East Asia); 16.72% (Eastern Pacific); 11.31% (Atlantic)]. The results are probably due to highly stable stratospheric air intruding into the mid-troposphere below the jet core by deep tropopause folding over East Asia (e.g., Kim & Chun, 2010), which inhibits lowered Ri due to the high values of N^2 . However, TI1, TI2, and TI3 diagnosed relatively higher probabilities of CAT potential mainly by strong VWS even in the highly stratified conditions over East Asia. These results will be further investigated using higher resolution reanalysis data and numerical simulations for CAT cases under strong VWS with highly stratified conditions (e.g., Kim & Chun, 2010; Trier et al., 2022).

Areas of negative PV (Fig. 3f) were concentrated mainly on the southern side of the climatological jets where inertial instability is generated by negative values of relative vorticity and Coriolis force decreases. The maximum frequency of negative PV was on the anticyclonic shear side of the East Asian jet and is mainly due to the negative values of relative vorticity generated by the strong jet streak over East Asia rather than convective instability (negative N^2 frequency is very small over East Asia; Fig. 3d). Therefore, East Asia is vulnerable to CAT caused by inertial/symmetric instability as well. The Eastern Pacific and Atlantic regions had low frequencies of PV on the anticyclonic shear side of the climatological jets. Over these regions, the occurrence of CAT by symmetric instability could be from convective instability since frequencies of N^2 are large due to storm tracks (Fig. 3d) if relative vorticity locally becomes positive.

Compared to winter, in summer (Figs. 5 and 6), the TI1, TI2, and TI3 frequencies were generally lower and shifted northward due to the weaker and northward shift of the mid-latitude jet stream. Local maxima of TI1, TI2, and TI3 still appear over East Asia, Northwest Atlantic and additionally over Mediterranean Europe in summer. As shown in Figure 6, the frequencies of the empirical indices components also decreased along the weakened jets in the NH. However, only the frequency of DEF (Fig. 6b) increased and displaced further north, which is consistent with the patterns of TI1, TI2, and TI3. Therefore, apparently DEF (Fig. 6b) has a larger impact than the

weakened VWS (Fig. 6a) on the occurrence of CAT at 250 hPa in the summer over the East Asian, Northwest Atlantic, and European regions. In addition, despite the weakened jets, higher frequencies of -DIV and DVT (Fig. 6c and 6d) than in winter were found over East Asia, which contributed to the maximum frequencies of TI1, TI2, and TI3 there. These may also be related to increased convective activity in this region than others as shown in Fig. 5d due to the summer monsoon system over East Asia (Yihui & Chan, 2005). In contrast, there were no increases in frequency patterns of -DIV and DVT in the Eastern Pacific and Atlantic regions unlike in winter because of the weakened jets and particularly the weakened storm tracks in the UTLS (Hoskins & Hodges, 2019). The summer distribution of CAT coincided well with the distribution of N^2 showing lower frequencies compared to the winter period over these regions. However, there were still relatively high frequencies of -DIV and DVT over North America but lower than in the winter period, which probably derived from mesoscale convective systems developing in this area in the summertime (Prein et al., 2020; Tian et al., 2005). Consequently, in summer as in winter, East Asia still has the highest CAT potential based on the empirical diagnostics.

These results were also identified in the theoretical instability diagnostics. In particular, the Ri distribution in summer (Fig. 5e) is distinctly different than in winter and is similar to the distribution of the empirical indices with local maxima over East Asia regardless of the weakened VWS (Fig. 6a). This is due to convectively low stability associated with the presence of the East Asian monsoon as mentioned above. Similarly, North America has a relative maximum in the frequency pattern of Ri which can be attributed to low stability generated by deep convection rather than weakened shear instability. The higher frequencies of negative PV were on the southern side of the summer jets in the NH but much lower frequencies than in winter due to decreased frequencies of negative absolute vorticity associated with the weaker jets.

3.3 Vertical Distribution

To further demonstrate the relationship between the jet system structures and CAT potential induced by various mechanisms in the UTLS, we display vertical cross sections of the CAT indices and their components in Figures 7-10. Here, we investigated four zonally averaged regions manifesting significant patterns of CAT potential in the horizontal distributions during the winter and summer periods.

In Fig. 7b over East Asia, the strongest jet cores with zonal wind speed exceeding 50 m s^{-1} are located between 100 and 500 hPa in winter. Accordingly, VWS, -DIV, and DVT became more frequent (Fig. 8b) with the maximum frequencies of the empirical indices (i.e., TI1, TI2, and TI3) above and below the jet core. Especially, VWS showed the highest frequencies at all levels among other midlatitude regions due to the strongest East Asian jet (maximum frequency of Europe = 20.0%; East Asia = 45.4%; Eastern Pacific = 28.9%; Atlantic = 17.1% from 100 hPa to 500 hPa in the 20-60°N; not shown). The high frequency of these large shears at all levels indicates high turbulence potential not only at the typical aircraft cruising levels of 250 hPa but also at other levels where aircraft travel over East Asia. In summer, the TI1, TI2, and TI3 distributions decreased and are shifted upward and northward along the weakened jet stream (Fig. 9b). However, unlike in the winter season, VWS is decreased by the weakened jet stream and DEF becomes more dominant from midlatitudes to polar regions at cruising levels as the jet core shifted upward (Fig.

10b). Moreover, -DIV and DVT are broadly distributed at cruising levels at low latitudes of East Asia because of the East Asia monsoon. Due to the increased frequency of DVT, isolated patterns of TI3 at upper-levels and low latitudes of East Asia (10-30°N, 160-120 hPa) were also found. Consequently, DEF, -DIV, and DVT largely contributed to the occurrence of CAT rather than VWS in the summer.

Over the Eastern Pacific and Northwestern Atlantic regions where jets were widely spread in the meridional direction, TI1, TI2, and TI3 were also distributed broadly from the south to north side of the jets (Fig. 7c and 7d). These are roughly equally due to DEF, VWS, -DIV, and DVT at 250 hPa (Fig. 8c and 8d). However, on the northern side of jet at lower levels below 250 hPa, DEF is expected to have the greatest impact on the occurrence of CAT. In summer, the areas of frequencies of TI1, TI2, and TI3 were generally smaller and shifted to the north along the weakened jet (Fig. 9c and 9d). It appears DEF was responsible for the CAT at cruising levels in summer over these regions because VWS was weakened and DEF was frequent on the northern side of the jet as was in East Asia (Fig. 10c and 10d). Areas of -DIV and DVT also decreased in summer due to fewer storm tracks, which is consistent with horizontal distributions in Eastern Pacific and Northwest Atlantic regions (Fig. 6c and 6d).

Over Europe in winter, two maxima of empirical indices were found because of the separate subtropical (20-30°N) and polar (50-60°N) jets, leading to two maxima in the patterns of TI1, TI2, and TI3 under each jet core (Fig. 7a). The patterns of TI1, TI2, and TI3 found at lower levels of the polar jet region (Fig. 7a) are related to DEF on the cyclonic shear side of the subtropical jet rather than VWS (Fig. 8a). On the other hand, the other maxima of TI1, TI2, and TI3 in the subtropical region (Fig. 7a) are primarily associated with VWS where the stronger jet stream developed (Fig. 8a). The two maxima frequencies of TI1, TI2, and TI3 were decreased in summer (Fig. 9a) due to the weakened and northward shifted subtropical jet that moved up to 30-40°N. Unlike in winter, maxima patterns of TI1, TI2, and TI3 found at upper levels above the polar jet (Fig. 9a) were mainly attributed to VWS (Fig. 10a).

In terms of the theoretical instability indices, areas of lowered Ri maxima were found over the Eastern Pacific and Northwest Atlantic regions (Fig. 7c and 7d) consistent with the higher frequencies of negative N^2 and larger VWS (Fig. 8c and 8d) there. However, despite the presence of large VWS at all levels (Fig. 8b), lowered Ri occurs only in the troposphere below 250 hPa in the midlatitudes of East Asia (Fig. 7b), while TI1, TI2, and TI3 were found at higher levels even above the tropopause indicated by the yellow dashed line. This is because the tropopause folding penetrated more deeply down to 300 hPa in the 30-40°N over East Asia than in other regions (vertically erected structure of yellow dashed line), which inhibits lowered Ri due to the extremely statically stable condition over this area (i.e., tropopause folding; Kim & Chun, 2010, 2011). Finally, hydrostatically high stability contributes to high values of Ri that is ambiguous to diagnose CAT induced by strong VWS at upper levels over East Asia in the winter. In contrast, as the tropopause shifted upward with a smaller jet in the summer, the stability of cruising levels within the subtropical and midlatitude regions over East Asia became low as shown in the distribution of N^2 (Fig. 9b and 10b), which lowered Ri that may be a more appropriate index in the summer.

The subtropical areas of East Asia are also prone to CAT due to inertial/symmetric instabilities as shown in the maximum frequency of $PV < 0$ distributed up to 30°N in the winter period (white line in Fig. 7b) while other regions were not (white lines in Fig. 7a, 7c, and 7d). The

inertial/symmetric instability generated in the winter period over East Asia was due to negative absolute vorticity in the strong jet streak. However, despite the weakened jet stream and smaller regions of negative absolute vorticity in summer, negative PV regions still occurred near 30°N on the southern side of the jet (Fig. 9b). This is a consequence of low stability due to the upward shift of the tropopause and instability associated with the summer monsoon. Additionally, an easterly wind over subtropical East Asia (not shown) plays a role in generating negative PV at the UTLS.

3.4 Trends

After investigating the average CAT climatology, spatial frequencies and their possible generation mechanisms relative to upper-level jet systems in the NH, we performed trend analyses to identify possible temporal changes as they may be affected by climate change over the past 41 years. Here, we analyzed winter season trends only when CAT is usually connected to jet streams. As previously mentioned, upper-level jet systems coincide with the meridional temperature gradient (MTG) through the thermal-wind balance. Therefore, the location and intensity of jet stream may both change in a global warming scenario (e.g., Lorenz & DeWeaver, 2007; Williams & Joshi, 2013). To start then, we first computed the 41 years mean fields of MTG at 300-400 hPa (Fig. 11a) and horizontal wind speed (SPD) at 250 hPa (Fig. 11b). They present similar patterns implying that the upper-level jet structure is highly correlated with MTG and consequently larger VWS according to the thermal wind relation. Therefore, the DJF mean trends ($\text{K m}^{-1} \text{ year}^{-1}$) of MTG at 300-400 hPa (Fig. 11d) that is modulating the jet stream at 250 hPa for the 41 years was examined. Here, we computed every 41 years DJF mean of MTG and then calculated the trend using a linear least-squares regression method (Lee et al., 2019). Statistically significant trend patterns were estimated at the 95% confidence levels ($P\text{-value} < 0.05$; $n = 41$) with a two-sided t -test (Lee et al., 2019) and these are indicated by black stippling as shown in Fig. 11d. Other variables of DJF mean trends and DJF mean frequency trends were computed in the same way.

The largest increase of MTG was found over East Asia (maximum value of $0.08 \text{ K m}^{-1} \text{ year}^{-1}$; 80-150°E, 30-45°N), which is slightly on the northern side of the East Asian jet entrance region (Fig. 11d). This is due to cooling in the middle Eurasian continent and warming in southeastern Asia regions (Fig. 11c) (e.g., He et al., 2020; Kug et al., 2015; Luo et al., 2017; J. Zhang et al., 2016). Positive increases were also seen over the Eastern Pacific (maximum value of $0.03 \text{ K m}^{-1} \text{ year}^{-1}$; 170°E-130°W, 35-55°N) and Atlantic (maximum value of $0.02 \text{ K m}^{-1} \text{ year}^{-1}$; 80-20°W, 35-60°N) regions (Fig. 11d) where strong warming in the tropics and lower latitude regions have occurred (Fig. 11c). Thus, as shown in Fig. 11e, the jet stream has strengthened and the wind speed has increased up to 0.16 m s^{-1} per year over East Asia and 0.13 m s^{-1} , 0.10 m s^{-1} per year over the Eastern Pacific and Atlantic due to global warming (e.g., Maloney et al., 2014; Sheffield et al., 2013). Also, from Fig. 11e, it is apparent that the midlatitude jets have shifted northward as well as intensified.

Time series of DJF means of MTG and SPD and their trends are displayed in Figure 12 over the three regions indicated by the red boxes in Figure 11 where large variations of trends were detected. The time series of MTG and SPD were calculated by annually (for DJF) averaging each variable over a designated area and then performing a simple linear regression to assess the trends. Over East Asia (Fig. 12a) where the strongest jets exist, MTG has increased by 10.87% ($P =$

0.025K m⁻¹ year⁻¹; P is slope of the regression line) and SPD has increased by 8.01% (P = 0.083m s⁻¹ year⁻¹) over the 41year period. Over the Eastern Pacific region (Fig. 12b), MTG increased 7.59% (P = 0.008K m⁻¹ year⁻¹) and SPD increased 6.86% (P = 0.056m s⁻¹ year⁻¹). Over the Atlantic region (Fig. 12c), MTG increased 3.38% (P = 0.004K m⁻¹ year⁻¹) and SPD increased 3.04% (P = 0.026m s⁻¹ year⁻¹).

The trends in CAT indices are shown in Figure 13. Overall, the trend patterns of CAT indices affected by jet systems were demonstrated with SPD trend at 250 hPa, as expected. Figure 14 shows box plots of increasing values of the turbulence diagnostics with time for three regions shown in Fig. 11. The box plots were calculated by regionally averaging the trends of each CAT index within designated areas shown in Figure 13. Again, East Asia showed the largest trend increases overall with TI1 increasing by 0.053% year⁻¹, TI2 by 0.048% year⁻¹, and TI3 by 0.054% year⁻¹, all mainly due to a large increase in VWS trend 0.080% year⁻¹, as shown in Fig. 13e and 14a. The Eastern Pacific had increases in TI1 of 0.034% year⁻¹, TI2 of 0.029% year⁻¹, and TI3 of 0.033% year⁻¹ which largely driven by the trend in DEF (0.039% year⁻¹) rather than VWS (0.007% year⁻¹) (Fig. 13e, 13f, and 14b). Trends in the Atlantic region were similar to those over the Eastern Pacific region with increases of TI1 by 0.039% year⁻¹, TI2 by 0.034% year⁻¹, and TI3 by 0.039% year⁻¹ driven mainly by trends in both VWS (0.032% year⁻¹) and DEF (0.036% year⁻¹) as shown in Fig. 13e, 13f, and 14c.

In contrast, the increased trend of Ri was the highest over the Eastern Pacific region (0.048% year⁻¹) with the lowest increase of VWS (Fig. 14b). We speculate that this may be due to increased Kelvin-Helmholtz instabilities by lowered static stability (small but positive trend in N² negative conditions were found for all regions in Figure 14) associated with the frequent development of cyclones along the storm tracks there. East Asia (0.022% year⁻¹) and the Atlantic (0.018% year⁻¹) regions also had Ri increases, which corresponds to strengthened VWS over each area. East Asia showed a relatively low increase of Ri even though VWS has intensified the most over the past 41 years. As previously mentioned, extremely statically stable condition from deep tropopause folding could disturb the identification of the shear instability trend diagnosed by Ri in UTLS over East Asia. In the case of PV, positive trends appeared along the intensified jet stream that intensifies the anticyclonic flows on the southern side of the jet. Additionally, as anticyclonic flow regions move northward, the largest reductions of PV occurred in the 20-30°N band over East Asia where maxima frequencies exist as shown in Fig. 3f.

4 Summary and Conclusions

In this study, climatologies of MOG-level CAT in the UTLS were discussed using high-resolution reanalysis ERA5 data for 41 years in the NH. To identify the occurrences of CAT and their various mechanisms near upper-level jets, the empirical (TI1, TI2, TI3, VWS, DEF, -DIV, and DVT) and theoretical instability (Ri, PV, and N²) diagnostics were used. The frequency distributions and trends of empirical diagnostics were investigated based on the thresholds

determined by calculating the top five percentile PDF value of each index at 250 hPa in the 20-60°N latitude band where long-haul flights cruise and the climatological jet stream exists.

Results showed that high frequencies of empirical indices occurred on the northern side of the jet in the winter period (DJF) and three maxima patterns were found over East Asia, Eastern Pacific, and Northwest Atlantic regions. The East Asia maxima coincides with the entrance of the strongest East Asian jet and has the highest frequencies in TI1, TI2, and TI3 mainly due to VWS. The Eastern Pacific and Atlantic regions also have high frequencies of TI1, TI2, and TI3 largely attributed to DEF, -DIV, and DVT at the exit of the jet stream as well as VWS. Over these regions, the patterns of lowered Ri were consistent with the patterns of N^2 and VWS indicating low static stability by induced by storm tracks and large shear instability at the exit region of the jet, respectively. On the other hand, Ri showed a minimum frequency over East Asia despite the highest frequency of VWS since the highly stable condition associated with stratospheric intrusion of stable air in the deep tropopause folds makes the value of Ri higher. The frequencies of negative PV were high on the southern side of the jet by negative relative vorticity and the maximum pattern occurred over East Asia where the strongest jet streak exists. We additionally found that the high resolution of the ERA5 data can possibly detect the potential of mountain wave turbulence from the distribution of DEF, -DIV, and DVT. In summer, the overall occurrence frequencies of MOG-level CAT were decreased and shifted poleward due to the north shifted and weakened jet stream in the NH. During this season, the three maxima patterns of TI1, TI2, and TI3 were found over East Asia, Northwest Atlantic, and Mediterranean Europe mainly impacted by increased DEF. Particularly East Asia had the highest CAT potential again in summer, which is primarily related to the summer monsoon system.

Next, to understand the location and intensity change of the jet stream, which leads to alteration of CAT occurrence in the UTLS, we identified a relation between SPD at 250 hPa and MTG at 300-400 hPa. As a consequence, there was an agreement between mean fields of MTG at 300-400 hPa and SPD at 250 hPa for 41 years suggesting upper-level jet structure is highly correlated with MTG by strengthening VWS according to thermal wind relationship. Therefore, increasing and decreasing trend patterns of SPD at 250 hPa over the past 41 years were correlated with those of the MTG trend at 300-400 hPa. The most significant increasing trend of the jet stream was found over East Asia primarily due to the enhanced VWS. It is associated with the largest increase trend of MTG over this region mainly due to cooling in the middle of the eastern Eurasian continent and warming in the southeastern Asia region. Finally, the potential of MOG-level CAT has increased the most significantly over East Asia along the intensified jet and associated increase in VWS. Relatively large increase trends of CAT potential also appeared over the Eastern Pacific and Northwest Atlantic regions enhanced by DEF and by both VWS and DEF respectively, which are likely due to global warming trends in these regions (e.g., Lee et al. 2019). Based on the trend patterns of CAT indices over the past 41 years, it is expected that MOG-level CAT encounters at cruising altitudes will be more common over East Asia with climate change. This trend will have a significant impact on a safe transpacific flight since a dense area of air traffic across the Pacific between East Asia and the US is highly collocated with the increasing trend of VWS causing MOG-level CAT as shown in Figure 15. An EDR density map was computed by counting the number of EDR values greater than zero based on Aircraft Meteorological Data Relay (AMDAR) observation data covering from January 2016 to September 2021 (Fig. 15). Therefore, it is

necessary to understand the generation mechanisms of MOG-level CAT events with these trends, especially over East Asia for efficient and safe aviation operations.

We expect that this study would help to understand the response of frequency distributions and trends of CAT that occur from various mechanisms in the NH to climate change. Given that the number of flights has increased consistently over the past years, and is expected to continue increasing, realizing a linkage between climate change and aviation turbulence becomes more important. Furthermore, we suggest that further study of climatology in cloud-induced turbulence and mountain wave turbulence which are also major sources of aviation turbulence (Doyle et al., 2005; J.-H. Kim et al., 2014; J.-H. Kim & Chun, 2011) is needed. Though they were not covered in this study, they also might be highly sensitive to climate change. Finally, the climatology of CAT based on observational data will be proceeded to examine whether it is consistent with the results analyzed by reanalysis data (e.g., Tenenbaum et al., 2022).

Acknowledgments, Samples, and Data

- The fifth generation ECMWF reanalysis hourly data (ERA5) on pressure levels can be downloaded at <https://cds.climate.copernicus.eu/cdsapp#!/dataset/10.24381/cds.bd0915c6?tab=overview>.
- Aircraft Meteorological Data Reports (AMDAR) data can be accessed from <https://data.eol.ucar.edu/dataset/100.016>.
- This work was supported by the Basic Science Research Program through the National Research Foundation of Korea (NRF), funded by the Ministry of Education (NRF-2019R1I1A2A1060035) and the Korea government (MSIT). This work also performed by the National Research Foundation of Korea (NRF) grant funded by the Korea government (MSIT) (No. NRF-2021R1A4A5032320).

References

- Abarbanel, H. D. I., Holm, D. D., Marsden, J. E., & Ratiu, T. (1984). Richardson Number Criterion for the Nonlinear Stability of Three-Dimensional Stratified Flow. *Physical Review Letters*, 52(26), 2352–2355. <https://doi.org/10.1103/PhysRevLett.52.2352>
- Cho, J. Y. N., & Lindborg, E. (2001). Horizontal velocity structure functions in the upper troposphere and lower stratosphere: 1. Observations. *Journal of Geophysical Research: Atmospheres*, 106(D10), 10223–10232. <https://doi.org/10.1029/2000JD900814>
- COLSON, D. (1963). ANALYSIS OF CLEAR AIR TURBULENCE DATA FOR MARCH 1962. *Monthly Weather Review*, 91(2), 73–82. [https://doi.org/10.1175/1520-0493\(1963\)091<0073:AOCATD>2.3.CO;2](https://doi.org/10.1175/1520-0493(1963)091<0073:AOCATD>2.3.CO;2)

- 536 Doyle, J. D., Shapiro, M. A., Jiang, Q., & Bartels, D. L. (2005). Large-Amplitude Mountain
537 Wave Breaking over Greenland. *Journal of the Atmospheric Sciences*, 62(9), 3106–3126.
538 <https://doi.org/10.1175/JAS3528.1>
- 539 Dutton, J. A., & Panofsky, H. A. (1970). Clear Air Turbulence: A Mystery May Be Unfolding:
540 High altitude turbulence poses serious problems for aviation and atmospheric science.
541 *Science*, 167(3920), 937–944.
- 542 Ellrod, G. P. (1985). Detection of high level turbulence using satellite imagery and upper air
543 data. (D. United States. National Environmental Satellite and Information Service, Ed.).
544 Retrieved from <https://repository.library.noaa.gov/view/noaa/32485>
- 545 Ellrod, G. P., & Knapp, D. I. (1992). An Objective Clear-Air Turbulence Forecasting Technique:
546 Verification and Operational Use. *Weather and Forecasting*, 7(1), 150–165.
547 [https://doi.org/10.1175/1520-0434\(1992\)007<0150:AOCATF>2.0.CO;2](https://doi.org/10.1175/1520-0434(1992)007<0150:AOCATF>2.0.CO;2)
- 548 Ellrod, G. P., & Knox, J. A. (2010). Improvements to an Operational Clear-Air Turbulence
549 Diagnostic Index by Addition of a Divergence Trend Term. *Weather and Forecasting*,
550 25(2), 789–798. <https://doi.org/10.1175/2009WAF2222290.1>
- 551 He, S., Xu, X., Furevik, T., & Gao, Y. (2020). Eurasian Cooling Linked to the Vertical
552 Distribution of Arctic Warming. *Geophysical Research Letters*, 47(10), e2020GL087212.
553 <https://doi.org/https://doi.org/10.1029/2020GL087212>
- 554 Holton, J. (n.d.). R.(1992), An Introduction to Dynamic Meteorology. *International Geophysics*
555 *Series*, 16.
- 556 Hoskins, B. J., & Hodges, K. I. (2019). The Annual Cycle of Northern Hemisphere Storm
557 Tracks. Part I: Seasons. *Journal of Climate*, 32(6), 1743–1760.
558 <https://doi.org/10.1175/JCLI-D-17-0870.1>
- 559 Jaeger, E. B., & Sprenger, M. (2007). A Northern Hemispheric climatology of indices for clear
560 air turbulence in the tropopause region derived from ERA40 reanalysis data. *Journal of*
561 *Geophysical Research: Atmospheres*, 112(D20).
562 <https://doi.org/https://doi.org/10.1029/2006JD008189>
- 563 Kim, J.-H., & Chun, H.-Y. (2010). A Numerical Study of Clear-Air Turbulence (CAT)
564 Encounters over South Korea on 2 April 2007. *Journal of Applied Meteorology and*
565 *Climatology*, 49(12), 2381–2403. <https://doi.org/10.1175/2010JAMC2449.1>
- 566 Kim, J.-H., & Chun, H.-Y. (2011). Statistics and Possible Sources of Aviation Turbulence over
567 South Korea. *Journal of Applied Meteorology and Climatology*, 50(2), 311–324.
568 <https://doi.org/10.1175/2010JAMC2492.1>
- 569 Kim, J.-H., & Chun, H.-Y. (2012). A Numerical Simulation of Convectively Induced Turbulence
570 above Deep Convection. *Journal of Applied Meteorology and Climatology*, 51(6), 1180–
571 1200. <https://doi.org/10.1175/JAMC-D-11-0140.1>

- Kim, J.-H., Chun, H.-Y., Sharman, R. D., & Keller, T. L. (2011). Evaluations of Upper-Level Turbulence Diagnostics Performance Using the Graphical Turbulence Guidance (GTG) System and Pilot Reports (PIREPs) over East Asia. *Journal of Applied Meteorology and Climatology*, 50(9), 1936–1951. <https://doi.org/10.1175/JAMC-D-10-05017.1>
- Kim, J.-H., Chun, H.-Y., Sharman, R. D., & Trier, S. B. (2014). The role of vertical shear on aviation turbulence within cirrus bands of a simulated western Pacific cyclone. *Monthly Weather Review*, 142(8), 2794–2813.
- Kim, J.-H., Chan, W. N., Sridhar, B., Sharman, R. D., Williams, P. D., & Strahan, M. (2016). Impact of the North Atlantic Oscillation on Transatlantic Flight Routes and Clear-Air Turbulence. *Journal of Applied Meteorology and Climatology*, 55(3), 763–771. <https://doi.org/10.1175/JAMC-D-15-0261.1>
- Kim, J.-H., Sharman, R., Strahan, M., Scheck, J. W., Bartholomew, C., Cheung, J. C. H., et al. (2018). Improvements in Nonconvective Aviation Turbulence Prediction for the World Area Forecast System. *Bulletin of the American Meteorological Society*, 99(11), 2295–2311. <https://doi.org/10.1175/BAMS-D-17-0117.1>
- Kim, J.-H., Kim, D., Lee, D.-B., Chun, H.-Y., Sharman, R. D., Williams, P. D., & Kim, Y.-J. (2020). Impact of climate variabilities on trans-oceanic flight times and emissions during strong NAO and ENSO phases. *Environmental Research Letters*, 15(10), 105017. <https://doi.org/10.1088/1748-9326/abaa77>
- Kim, S.-H., Kim, J., Kim, J.-H., & Chun, H.-Y. (2022). Characteristics of the derived energy dissipation rate using the 1 Hz commercial aircraft quick access recorder (QAR) data. *Atmos. Meas. Tech.*, 15(7), 2277–2298. <https://doi.org/10.5194/amt-15-2277-2022>
- Knox, J. A. (1997). Possible Mechanisms of Clear-Air Turbulence in Strongly Anticyclonic Flows. *Monthly Weather Review*, 125(6), 1251–1259. [https://doi.org/10.1175/1520-0493\(1997\)125<1251:PMOCAT>2.0.CO;2](https://doi.org/10.1175/1520-0493(1997)125<1251:PMOCAT>2.0.CO;2)
- Knox, J. A., & Harvey, V. L. (2005). Global climatology of inertial instability and Rossby wave breaking in the stratosphere. *Journal of Geophysical Research: Atmospheres*, 110(D6). <https://doi.org/https://doi.org/10.1029/2004JD005068>
- Knox, J. A., McCann, D. W., & Williams, P. D. (2008). Application of the Lighthill–Ford Theory of Spontaneous Imbalance to Clear-Air Turbulence Forecasting. *Journal of the Atmospheric Sciences*, 65(10), 3292–3304. <https://doi.org/10.1175/2008JAS2477.1>
- Koch, S. E., Jamison, B. D., Lu, C., Smith, T. L., Tollerud, E. I., Girz, C., et al. (2005). Turbulence and Gravity Waves within an Upper-Level Front. *Journal of the Atmospheric Sciences*, 62(11), 3885–3908. <https://doi.org/10.1175/JAS3574.1>
- Kug, J.-S., Jeong, J.-H., Jang, Y.-S., Kim, B.-M., Folland, C. K., Min, S.-K., & Son, S.-W. (2015). Two distinct influences of Arctic warming on cold winters over North America and East Asia. *Nature Geoscience*, 8(10), 759–762. <https://doi.org/10.1038/ngeo2517>

- 609 Lane, T. P., Doyle, J. D., Plougonven, R., Shapiro, M. A., & Sharman, R. D. (2004).
610 Observations and Numerical Simulations of Inertia–Gravity Waves and Shearing
611 Instabilities in the Vicinity of a Jet Stream. *Journal of the Atmospheric Sciences*, 61(22),
612 2692–2706. <https://doi.org/10.1175/JAS3305.1>
- 613 Lee, D.-B., & Chun, H.-Y. (2015). A Statistical Analysis of Aviation Turbulence Observed in
614 Pilot Report (PIREP) over East Asia Including South Korea. *Atmosphere*, 25(1), 129–140.
615 <https://doi.org/10.14191/ATMOS.2015.25.1.129>
- 616 Lee, D.-B., Chun, H.-Y., & Kim, J.-H. (2020). Evaluation of Multimodel-Based Ensemble
617 Forecasts for Clear-Air Turbulence. *Weather and Forecasting*, 35(2), 507–521.
618 <https://doi.org/10.1175/WAF-D-19-0155.1>
- 619 Lee, S. H., Williams, P. D., & Frame, T. H. A. (2019). Increased shear in the North Atlantic
620 upper-level jet stream over the past four decades. *Nature*, 572(7771), 639–642.
621 <https://doi.org/10.1038/s41586-019-1465-z>
- 622 Lester, P. F. (1994). *Turbulence: A new perspective for pilots*. Jeppesen Sanderson.
- 623 Lorenz, D. J., & DeWeaver, E. T. (2007). Tropopause height and zonal wind response to global
624 warming in the IPCC scenario integrations. *Journal of Geophysical Research: Atmospheres*,
625 112(D10). <https://doi.org/https://doi.org/10.1029/2006JD008087>
- 626 Luo, D., Chen, Y., Dai, A., Mu, M., Zhang, R., & Ian, S. (2017). Winter Eurasian cooling linked
627 with the Atlantic Multidecadal Oscillation. *Environmental Research Letters*, 12(12),
628 125002. <https://doi.org/10.1088/1748-9326/aa8de8>
- 629 Lv, Y., Guo, J., Li, J., Han, Y., Xu, H., Guo, X., et al. (2021). Increased Turbulence in the
630 Eurasian Upper-Level Jet Stream in Winter: Past and Future. *Earth and Space Science*, 8(2),
631 e2020EA001556. <https://doi.org/https://doi.org/10.1029/2020EA001556>
- 632 Maloney, E. D., Camargo, S. J., Chang, E., Colle, B., Fu, R., Geil, K. L., et al. (2014). North
633 American Climate in CMIP5 Experiments: Part III: Assessment of Twenty-First-Century
634 Projections. *Journal of Climate*, 27(6), 2230–2270. <https://doi.org/10.1175/JCLI-D-13-00273.1>
- 636 Prein, A. F., Liu, C., Ikeda, K., Bullock, R., Rasmussen, R. M., Holland, G. J., & Clark, M.
637 (2020). Simulating North American mesoscale convective systems with a convection-
638 permitting climate model. *Climate Dynamics*, 55(1), 95–110.
639 <https://doi.org/10.1007/s00382-017-3993-2>
- 640 Sato, K., & Dunkerton, T. J. (2002). Layered Structure Associated with Low Potential Vorticity
641 near the Tropopause Seen in High-Resolution Radiosondes over Japan. *Journal of the*
642 *Atmospheric Sciences*, 59(19), 2782–2800. [https://doi.org/10.1175/1520-0469\(2002\)059<2782:LSAWLP>2.0.CO;2](https://doi.org/10.1175/1520-0469(2002)059<2782:LSAWLP>2.0.CO;2)

- Sharman, R., Tebaldi, C., Wiener, G., & Wolff, J. (2006). An Integrated Approach to Mid- and Upper-Level Turbulence Forecasting. *Weather and Forecasting*, 21(3), 268–287. <https://doi.org/10.1175/WAF924.1>
- Sharman, R. D., & Pearson, J. M. (2017). Prediction of Energy Dissipation Rates for Aviation Turbulence. Part I: Forecasting Nonconvective Turbulence. *Journal of Applied Meteorology and Climatology*, 56(2), 317–337. <https://doi.org/10.1175/JAMC-D-16-0205.1>
- Sharman, R. D., Trier, S. B., Lane, T. P., & Doyle, J. D. (2012). Sources and dynamics of turbulence in the upper troposphere and lower stratosphere: A review. *Geophysical Research Letters*, 39(12). <https://doi.org/https://doi.org/10.1029/2012GL051996>
- Sharman, R. D., Cornman, L. B., Meymaris, G., Pearson, J., & Farrar, T. (2014). Description and Derived Climatologies of Automated In Situ Eddy-Dissipation-Rate Reports of Atmospheric Turbulence. *Journal of Applied Meteorology and Climatology*, 53(6), 1416–1432. <https://doi.org/10.1175/JAMC-D-13-0329.1>
- Sheffield, J., Barrett, A. P., Colle, B., Nelun Fernando, D., Fu, R., Geil, K. L., et al. (2013). North American Climate in CMIP5 Experiments. Part I: Evaluation of Historical Simulations of Continental and Regional Climatology*. *Journal of Climate*, 26(23), 9209–9245. <https://doi.org/10.1175/JCLI-D-12-00592.1>
- Storer, L. N., Williams, P. D., & Joshi, M. M. (2017). Global Response of Clear-Air Turbulence to Climate Change. *Geophysical Research Letters*, 44(19), 9976–9984. <https://doi.org/https://doi.org/10.1002/2017GL074618>
- Tenenbaum, J., Williams, P. D., Turp, D., Buchanan, P., Coulson, R., Gill, P. G., et al. (2022). Aircraft observations and reanalysis depictions of trends in the North Atlantic winter jet stream wind speeds and turbulence. *Quarterly Journal of the Royal Meteorological Society*, n/a(n/a). <https://doi.org/https://doi.org/10.1002/qj.4342>
- Thompson, C. F., Schultz, D. M., & Vaughan, G. (2018). A Global Climatology of Tropospheric Inertial Instability. *Journal of the Atmospheric Sciences*, 75(3), 805–825. <https://doi.org/10.1175/JAS-D-17-0062.1>
- Tian, B., Held, I. M., Lau, N.-C., & Soden, B. J. (2005). Diurnal cycle of summertime deep convection over North America: A satellite perspective. *Journal of Geophysical Research: Atmospheres*, 110(D8). <https://doi.org/https://doi.org/10.1029/2004JD005275>
- Trier, S. B., & Sharman, R. D. (2016). Mechanisms Influencing Cirrus Banding and Aviation Turbulence near a Convectively Enhanced Upper-Level Jet Stream. *Monthly Weather Review*, 144(8), 3003–3027. <https://doi.org/10.1175/MWR-D-16-0094.1>
- Trier, S. B., Sharman, R. D., Muñoz-Esparza, D., & Keller, T. L. (2022). Effects of Distant Organized Convection on Forecasts of Widespread Clear-Air Turbulence. *Monthly Weather Review*. <https://doi.org/10.1175/MWR-D-22-0077.1>

Williams, P. D. (2017). Increased light, moderate, and severe clear-air turbulence in response to climate change. *Advances in Atmospheric Sciences*, 34(5), 576–586. <https://doi.org/10.1007/s00376-017-6268-2>

Williams, P. D., & Joshi, M. M. (2013). Intensification of winter transatlantic aviation turbulence in response to climate change. *Nature Climate Change*, 3(7), 644–648. <https://doi.org/10.1038/nclimate1866>

Wolff, J. K., & Sharman, R. D. (2008). Climatology of Upper-Level Turbulence over the Contiguous United States. *Journal of Applied Meteorology and Climatology*, 47(8), 2198–2214. <https://doi.org/10.1175/2008JAMC1799.1>

Yihui, D., & Chan, J. C. L. (2005). The East Asian summer monsoon: an overview. *Meteorology and Atmospheric Physics*, 89(1), 117–142. <https://doi.org/10.1007/s00703-005-0125-z>

Zhang, F. (2004). Generation of Mesoscale Gravity Waves in Upper-Tropospheric Jet–Front Systems. *Journal of the Atmospheric Sciences*, 61(4), 440–457. [https://doi.org/10.1175/1520-0469\(2004\)061<0440:GOMGWI>2.0.CO;2](https://doi.org/10.1175/1520-0469(2004)061<0440:GOMGWI>2.0.CO;2)

Zhang, J., Tian, W., Chipperfield, M. P., Xie, F., & Huang, J. (2016). Persistent shift of the Arctic polar vortex towards the Eurasian continent in recent decades. *Nature Climate Change*, 6(12), 1094–1099. <https://doi.org/10.1038/nclimate3136>

Figure 1. PDFs of each CAT index calculated at 250 hPa in the 20-60°N latitude band for 41 years (1979 – 2019). Red and blue histograms indicate summer and winter seasons, respectively, and orange shows the overlap region between the two seasons. The 95th percentile value is depicted by black dashed vertical line.

Figure 2. (a), (b) Horizontal wind speed (shading) with geopotential height (60gpm interval; gray contour) on 225 hPa at 0600 UTC and 1100 UTC Oct 2012 respectively. CAT indices distributions (c) TI1 = 9.07×10^{-7} (green dashed contour), TI2 = 1.03×10^{-6} (navy dashed-dotted contour), TI3 = 1.39×10^{-6} (purple dotted contour), PV = 0 (black solid bold contour), and Ri = 1 (orange solid contour), (d) VWS (shading) with zonal wind speed at 1100 UTC 11 October 2012 at 225hPa over eastern Japan. Zonal wind speed is shown by shading and gray contours in (c) and (d) respectively from 10 to 70 m s⁻¹ with a 10 m s⁻¹ interval. Black dashed contour in (d) represents the threshold of VWS (1.03×10^{-2}). Flight routes and locations of MOG turbulence at 1010 UTC and 1125 UTC 11 Oct 2012 are depicted by black solid thin lines and red [(a), (b), and (c)] and black [(d)] asterisks.

Figure 3. Frequency (%) distributions of CAT indices with shading (a) TI1, (b) TI2, (c) TI3, (d) N², (e) Ri, and (f) PV at 250 hPa in the 20-80°N for 41 years (1979 – 2019) for the winter period (DJF). Averaged zonal wind speeds are also shown as black contours from 30 to 80 m s⁻¹ at 10 m s⁻¹ intervals.

Figure 4. Frequency (%) distributions of CAT indices with shading (a) VWS, (b) DEF, (d) -DIV, and (d) DVT at 250 hPa in the 20-80°N for 41 years (1979 – 2019) for the winter period (DJF). Averaged zonal wind speeds are also shown as black contour from 30 to 80 m s⁻¹ at 10 m s⁻¹ intervals.

Figure 5. Same as Figure 3, but for the summer period (JJA). Distributions of averaged zonal wind speed are shown as black contours from 25 to 65 m s⁻¹ at 10 m s⁻¹ intervals.

Figure 6. Same as Figure 4, but for the summer period (JJA). Distributions of averaged zonal wind speed are shown as black contour from 25 to 65 m s⁻¹ at 10 m s⁻¹ intervals.

Figure 7. Vertical frequency distributions of zonally averaged CAT indices during the winter period (DJF) for 41 years (1979 – 2019) [TI1 = 5% (red dashed contour), TI2 = 5% (black dashed-dotted contour), TI3 = 5% (blue dotted contour), PV = 10% (white solid contour), and Ri = 5% (pink solid contour)] and zonal wind speed (shading from 0 to 50 m s⁻¹ at 5 m s⁻¹ interval) for 4 regions: Europe [10-50°E; (a)], East Asia [120-160°E; (b)], Eastern Pacific [180°E-140°W; (c)] and Atlantic [80-40°W; (d)]. Isentropes and 2 PVU tropopause are indicated by thin grey line and yellow dashed line respectively. White thin double dotted line represents altitude of 250 hPa.

Figure 8. Same as Figure7, but for [VWS = 6% (orange solid contour), DEF = 7.5% (green solid contour), -DIV = 3% (blue-green dashed-dotted contour), DVT = 5.5% (brown solid contour), and N² = 0.02% (white solid contour)] and zonal wind speed (shading from 0 to 50 m s⁻¹ at 5 m s⁻¹ interval)

Figure 9. Same as Figure 7, but for the summer period (JJA).

Figure 10. Same as Figure 8, but for the summer period (JJA).

Figure 11. (a) and (b) show averaged meridional temperature gradient (MTG) and horizontal wind speed (SPD) at 300-400 hPa and 250 hPa for 41 years (1979 – 2019) respectively with shading. DJF mean trends (shading) of (c) Temperature at 300-400 hPa, (d) Meridional temperature gradient at 300-400 hPa, and (e) Horizontal wind speed at 250 hPa. Black contour and stippling depict zonal wind speed at 250 hPa (from 30 to 80 m s⁻¹ with 10 m s⁻¹ interval) and significant trends (P-value < 0.05, n = 41). Red boxes in (c)-(e) indicate East Asia (80-150°E, 30-45°N), Eastern Pacific (170°E-130°W, 35-55°N), and Atlantic (80-20°W, 35-60°N) regions from the left.

Figure 12. Time series of DJF mean meridional temperature gradient MTG (pink solid line), linear trends of MTG (pink dashed line), DJF mean horizontal wind speed SPD (light blue solid line), and linear trends of SPD (light blue dashed line) over 3 regions (indicated by the red boxes in Fig. 11) (a) East Asia (80-150°E, 30-45°N), (b) Eastern Pacific (170°E-130°W, 35-55°N), and (c) Atlantic (80-20°W, 35-60°N) over 41 years (1979 – 2019).

Figure 13. DJF frequency trends at 250 hPa of (a) TI1, (b) TI2, (c) TI3, (d) Ri, (e) VWS, (f) DEF, (g) -DIV, (h) DVT, and (i) PV (shaded) for 41 years (1979 – 2019). Black contours and stippling depict zonal wind speed at 250 hPa (30 to 80 m s⁻¹ at 10 m s⁻¹ interval) and significant trends (P-value < 0.05, n = 41) respectively. Red boxes indicate regions same as Figure 11.

Figure 14. Box plots of 10 CAT indices over 3 regions (indicated by the red boxes in Figure 13) (a) East Asia (80-150°E, 30-45°N), (b) Eastern Pacific (170°E-130°W, 35-55°N), and (c) Atlantic (80-20°W, 35-60°N). The top and bottom of black line show the maximum and minimum frequency trend value of each index within each red box area. Red bars and black dot represent averaged frequency trend and median value of each index within each red box area respectively.

Figure 15. EDR (> 0m^{2/3}s⁻¹) distribution (shading) from AMDAR data with winter VWS trend (contour; negative values are indicated by dash contours) (from January 2016 to September 2021).

Figure1.

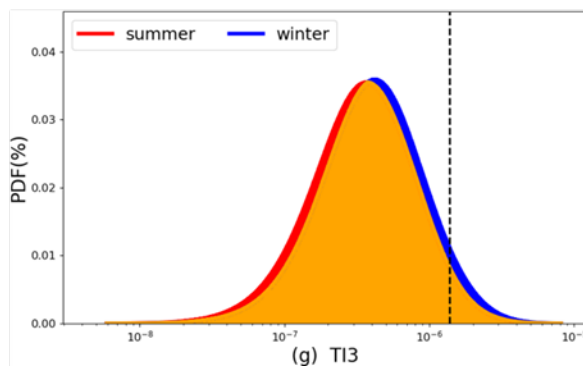
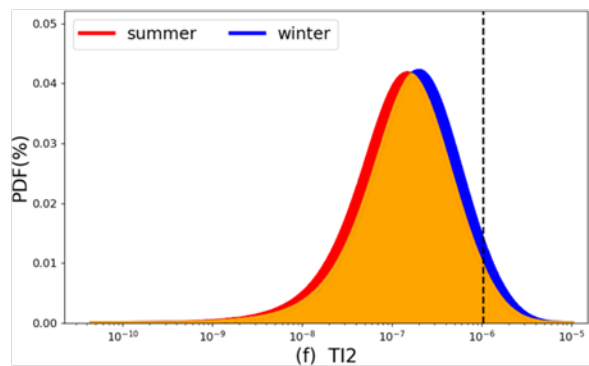
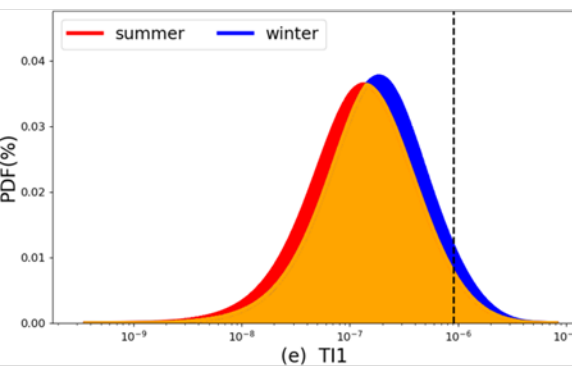
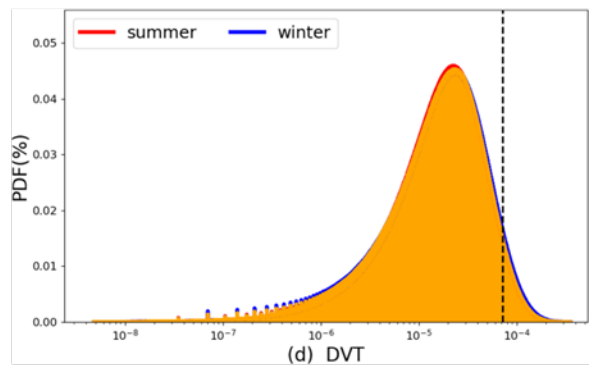
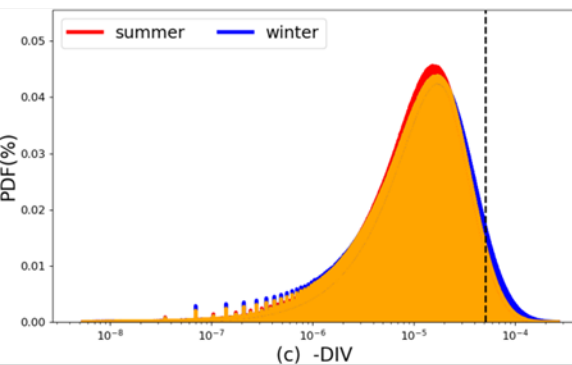
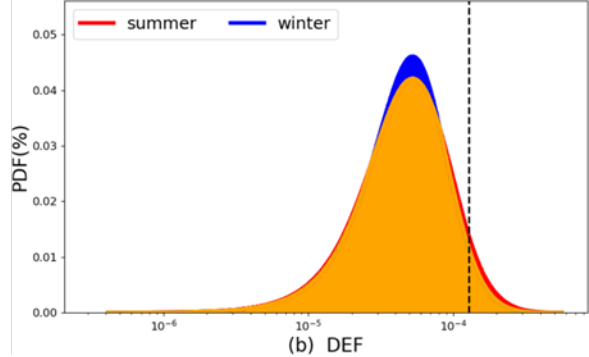
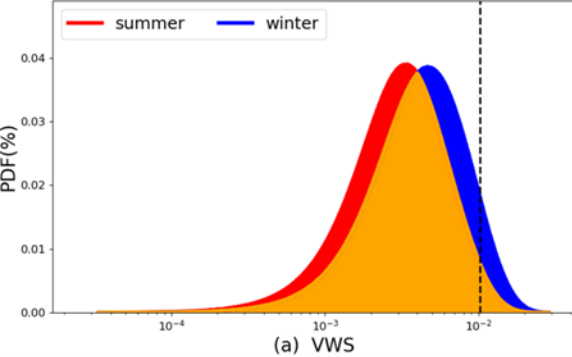
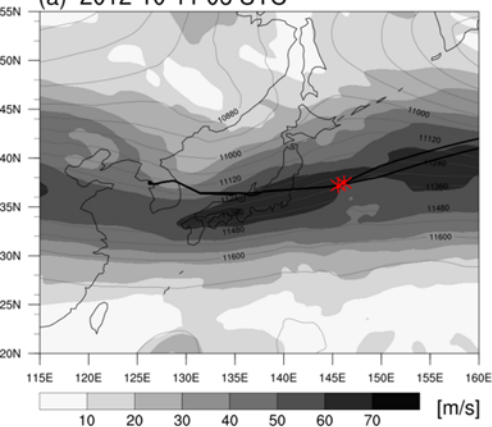
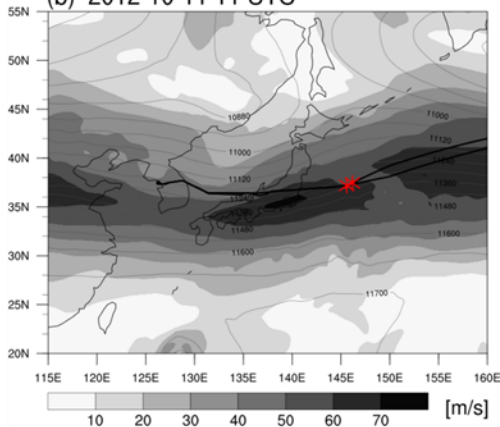


Figure2.

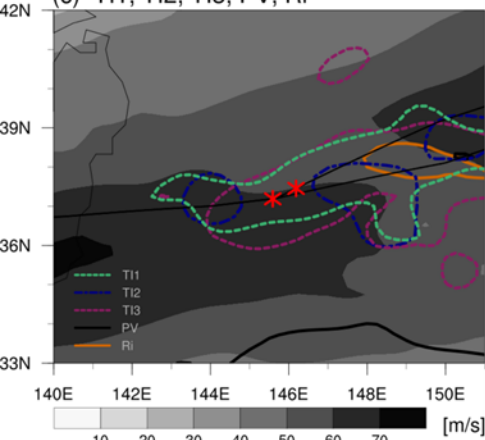
(a) 2012-10-11 06 UTC



(b) 2012-10-11 11 UTC



(c) TI1, TI2, TI3, PV, Ri



(d) VWS

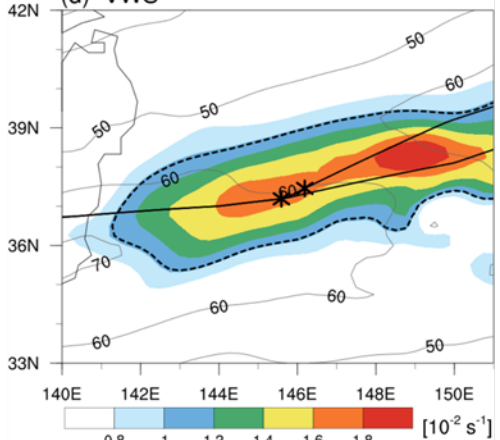
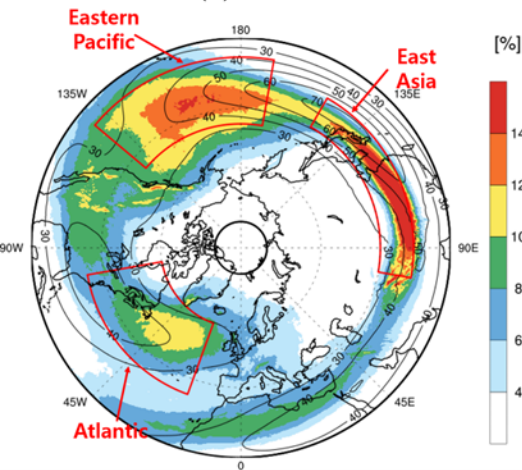
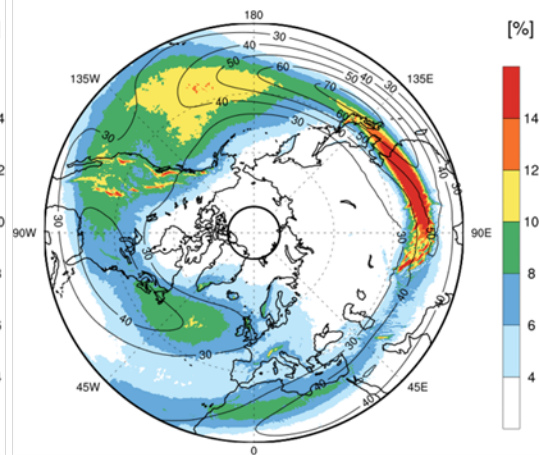


Figure3.

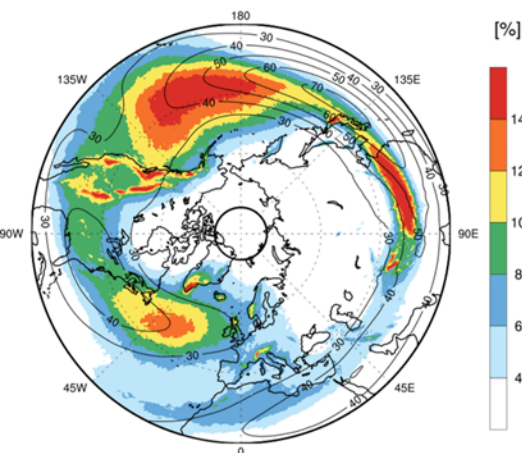
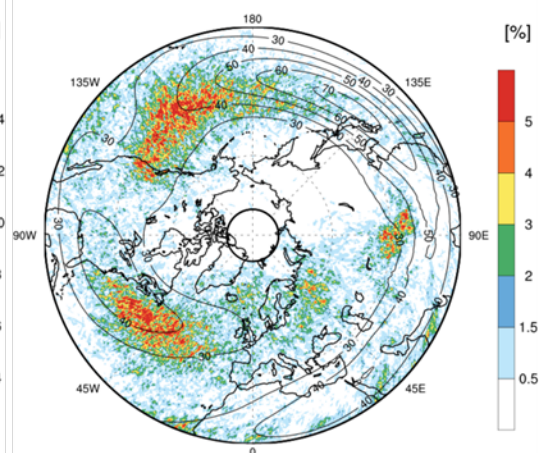
(a) TI1



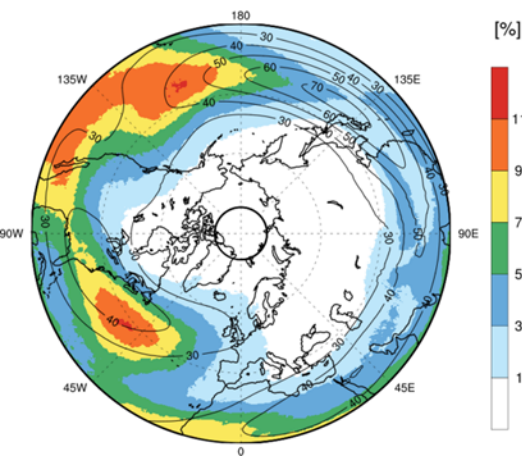
(b) TI2



(c) TI3

(d) N²

(e) Ri



(f) PV

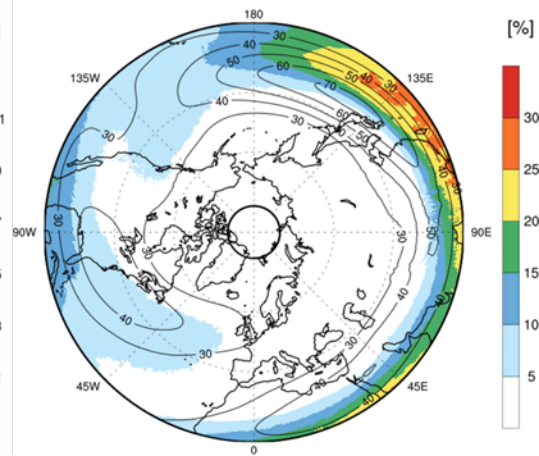
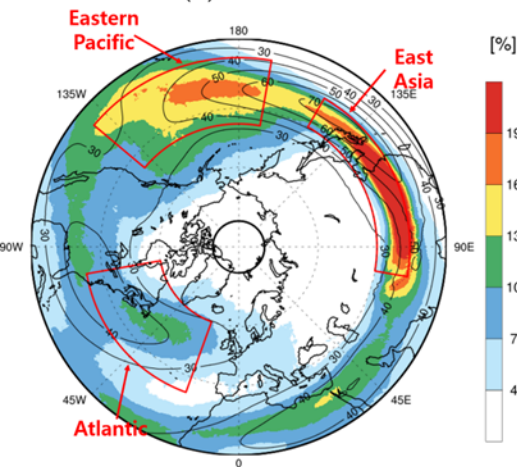
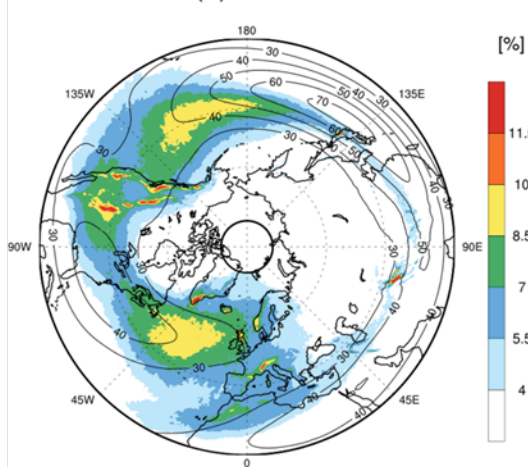


Figure4.

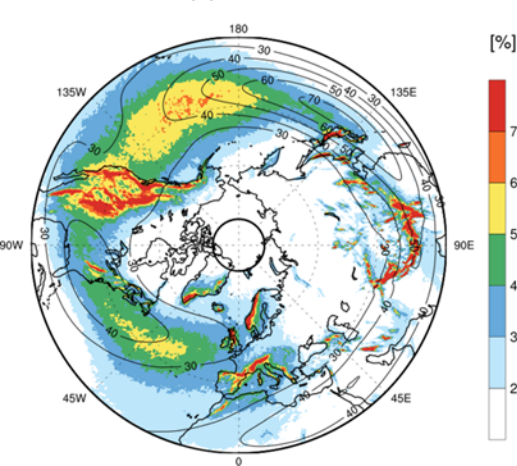
(a) VWS



(b) DEF



(c) -DIV



(d) DVT

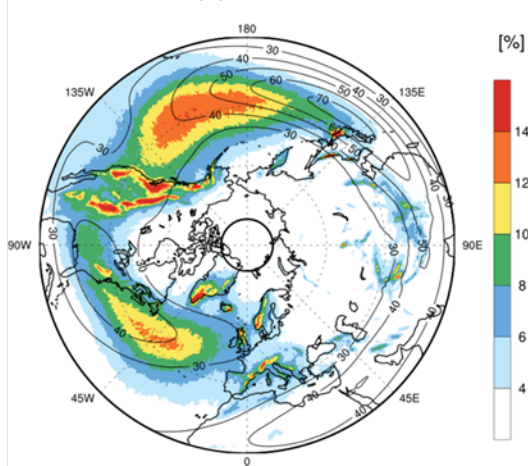
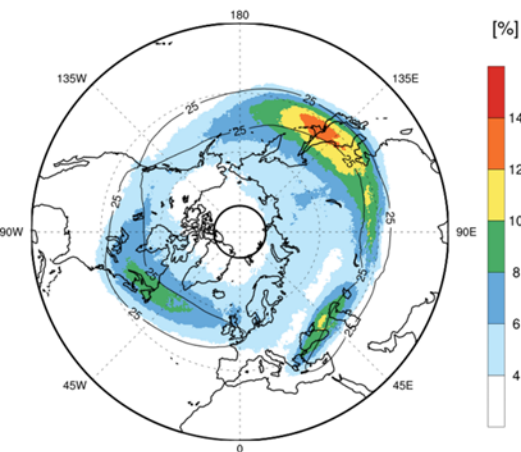
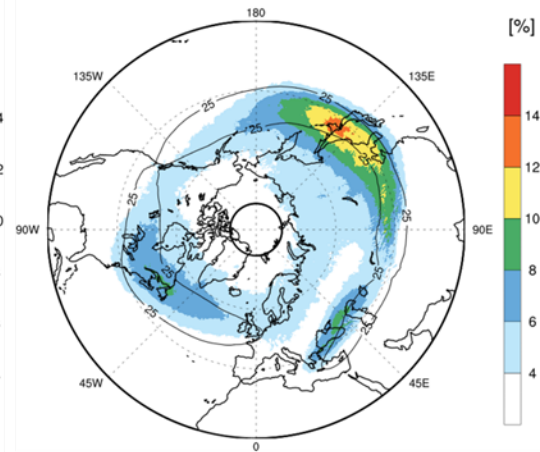


Figure5.

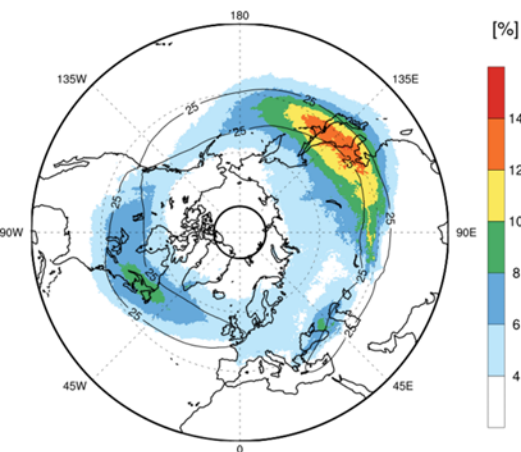
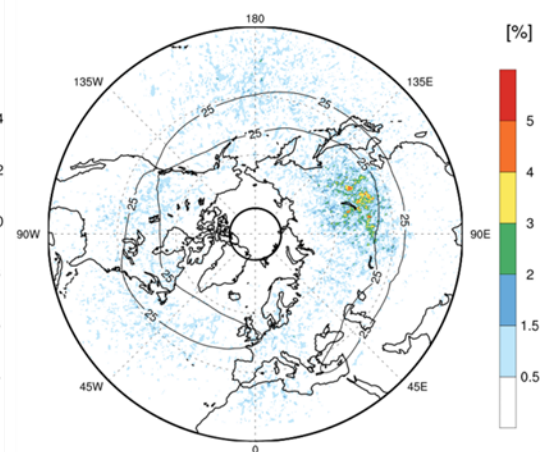
(a) TI1



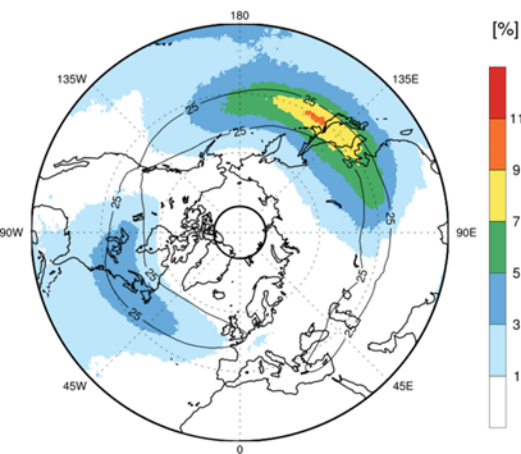
(b) TI2



(c) TI3

(d) N^2 

(e) Ri



(f) PV

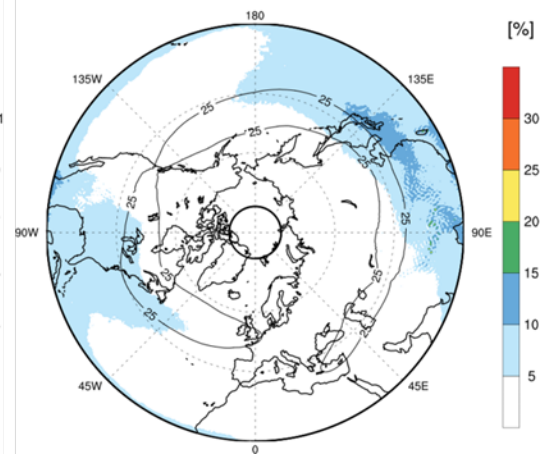
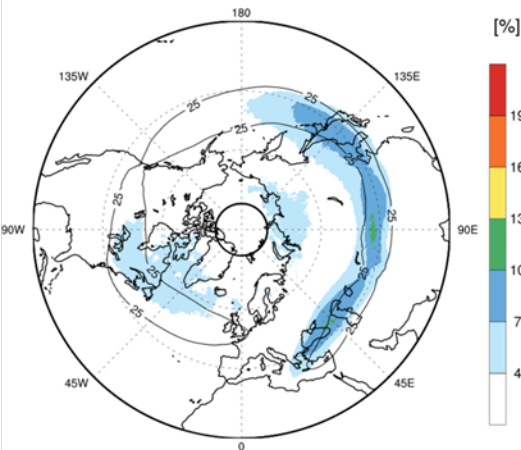
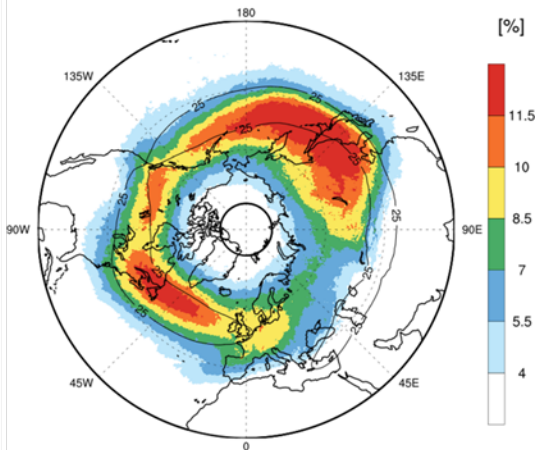


Figure6.

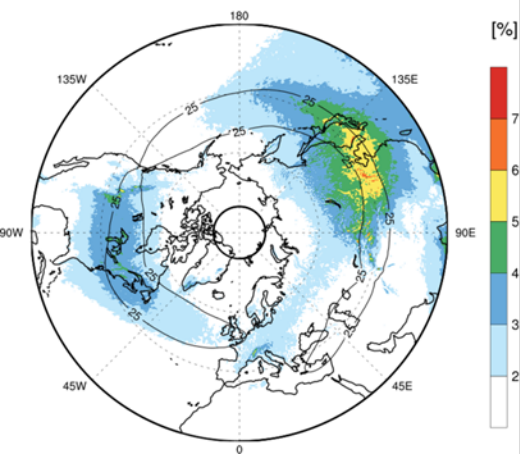
(a) VWS



(b) DEF



(c) -DIV



(d) DVT

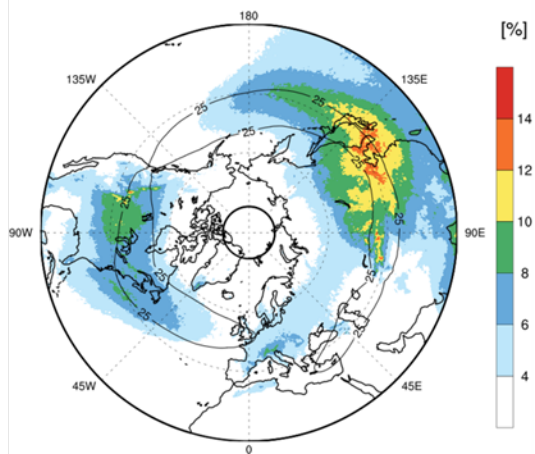


Figure7.

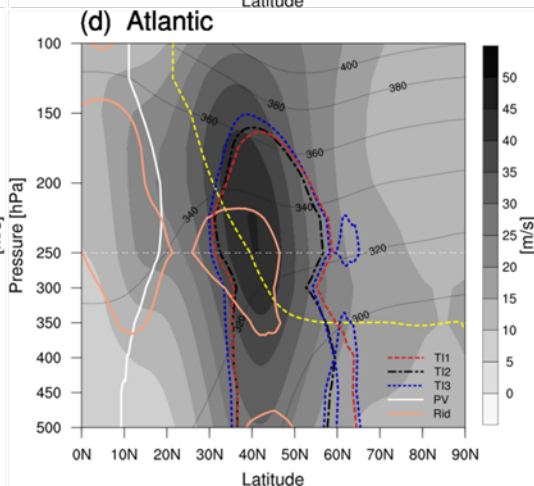
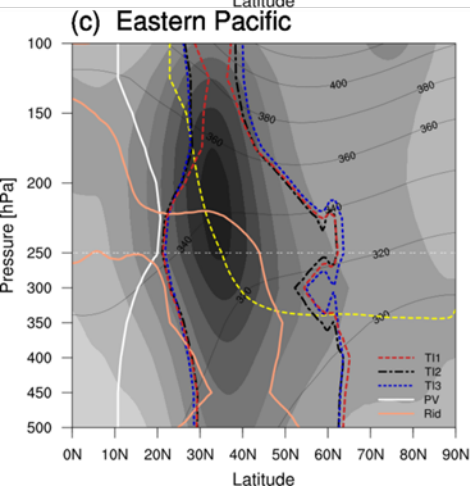
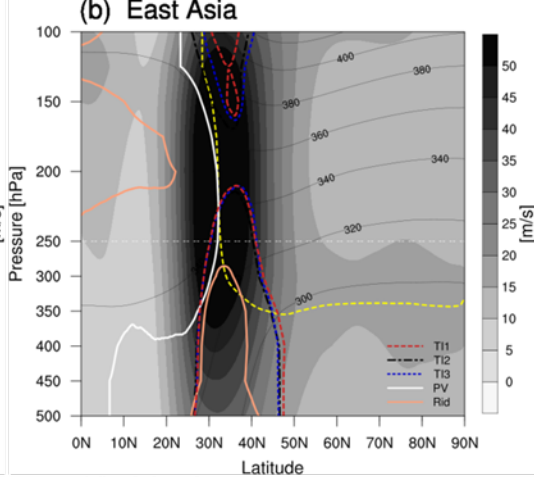
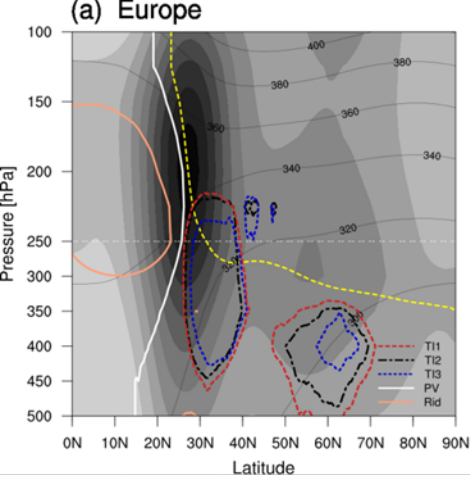


Figure8.

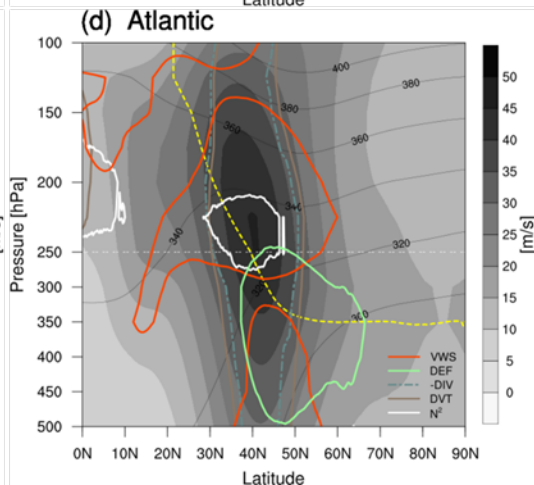
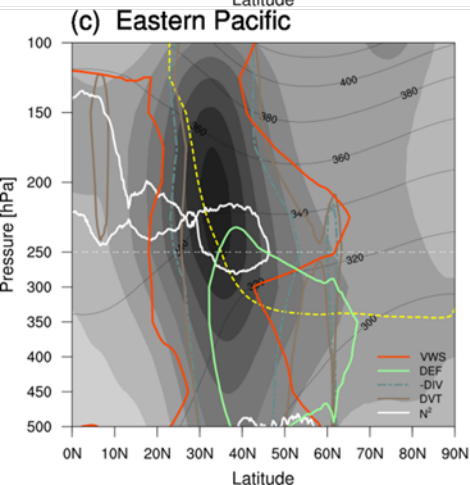
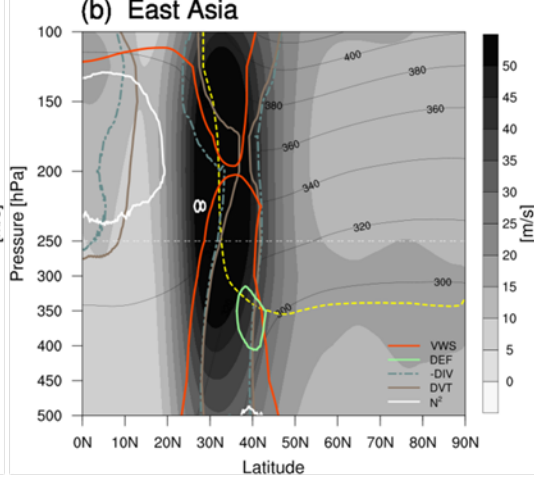
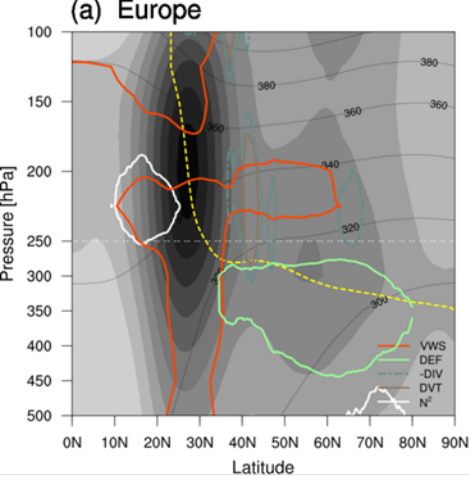


Figure9.

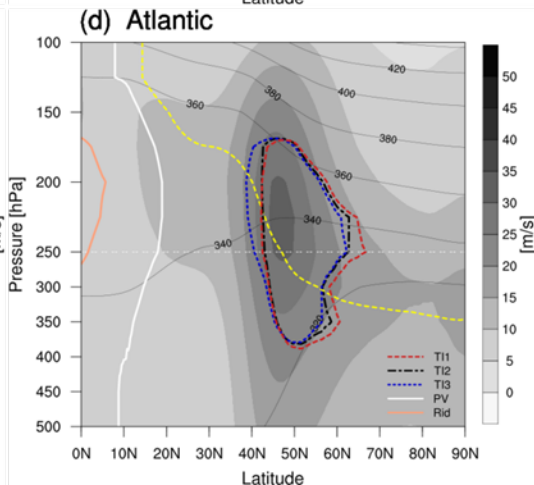
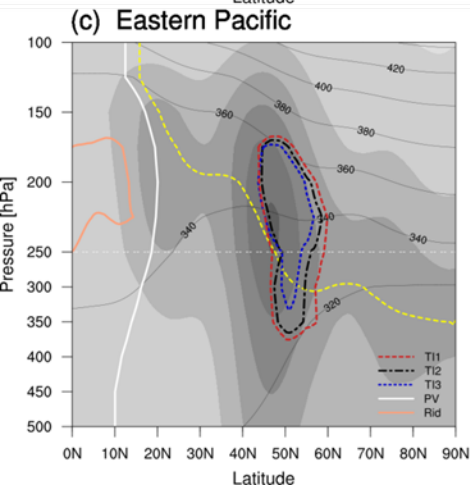
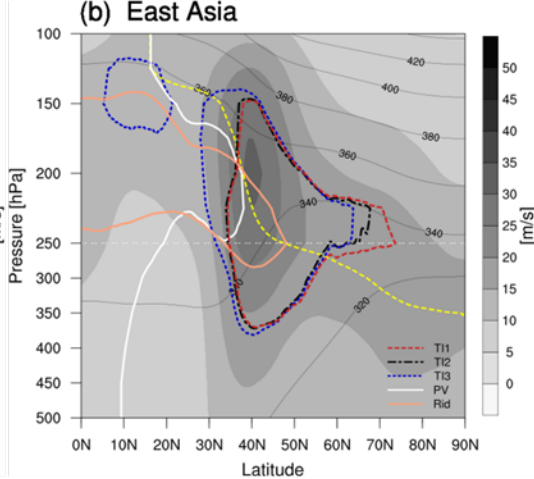
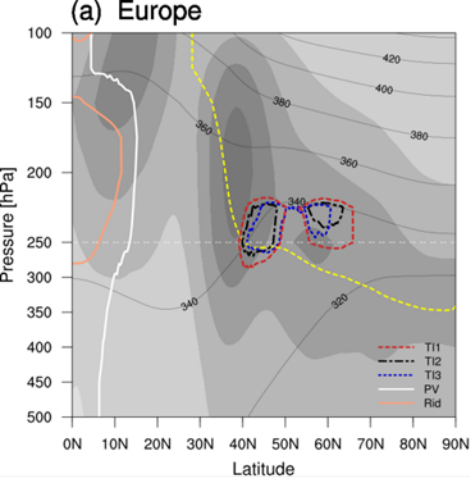


Figure10.

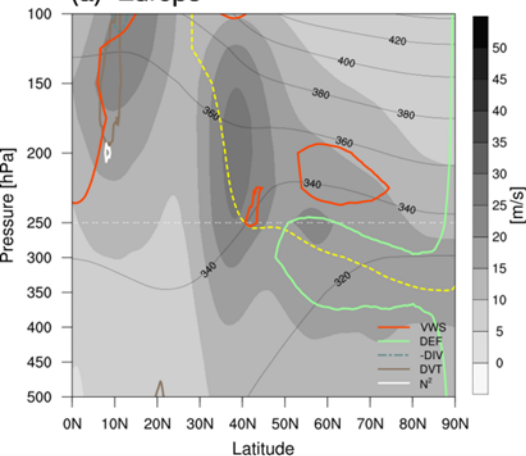
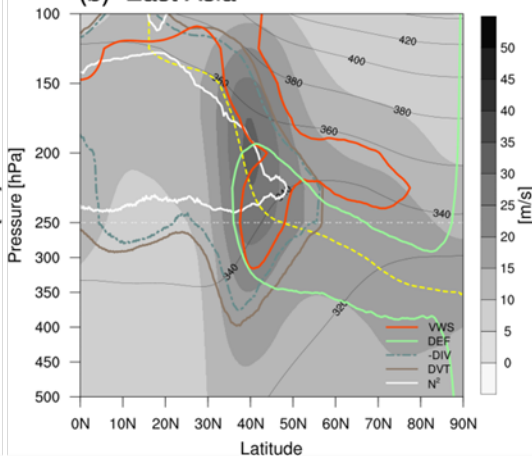
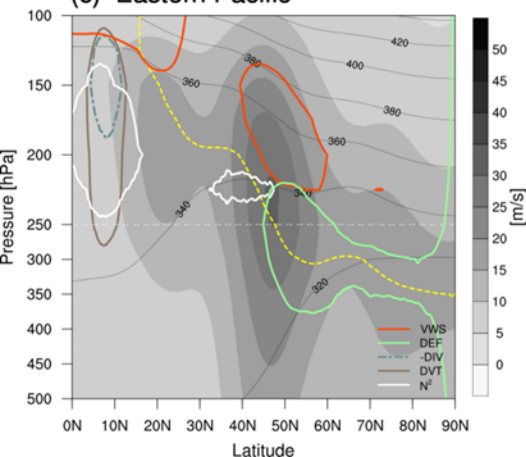
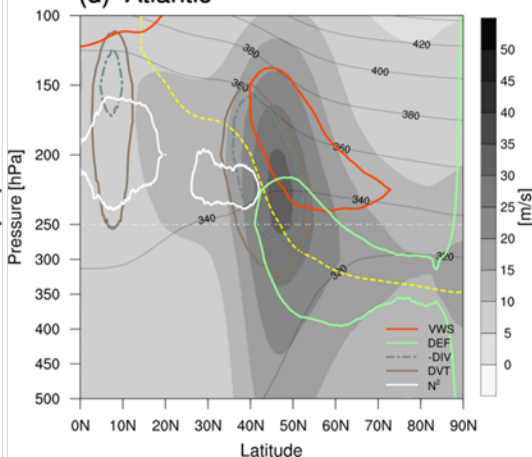
(a) Europe**(b) East Asia****(c) Eastern Pacific****(d) Atlantic**

Figure11.

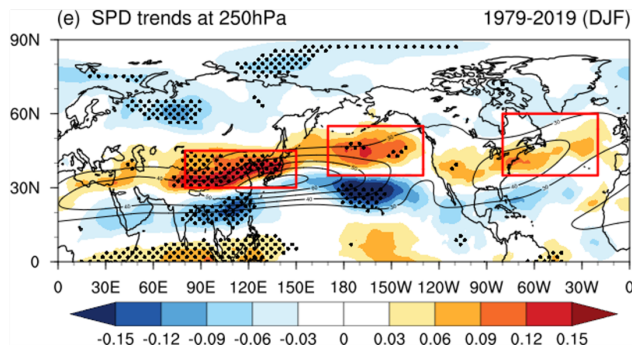
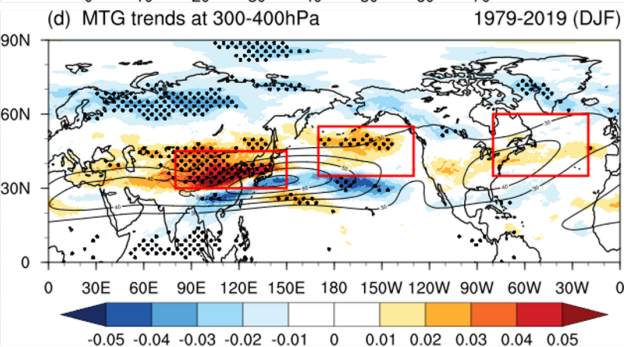
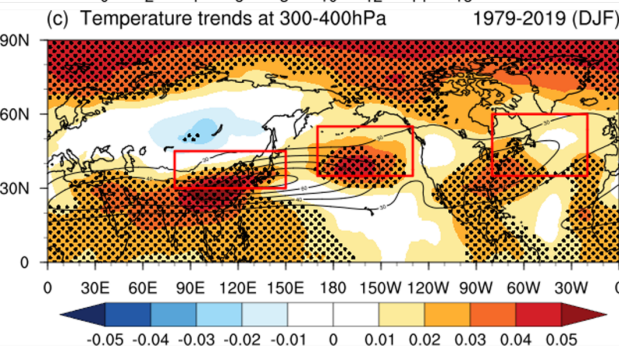
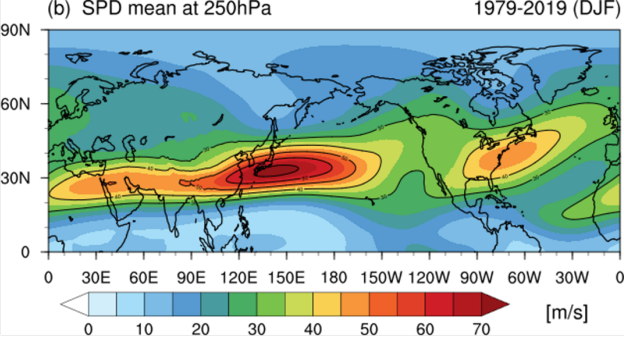
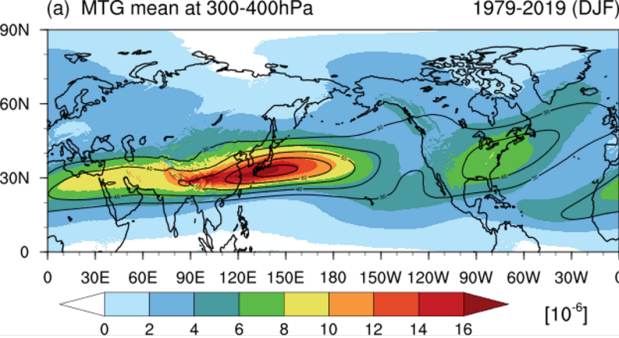


Figure12.

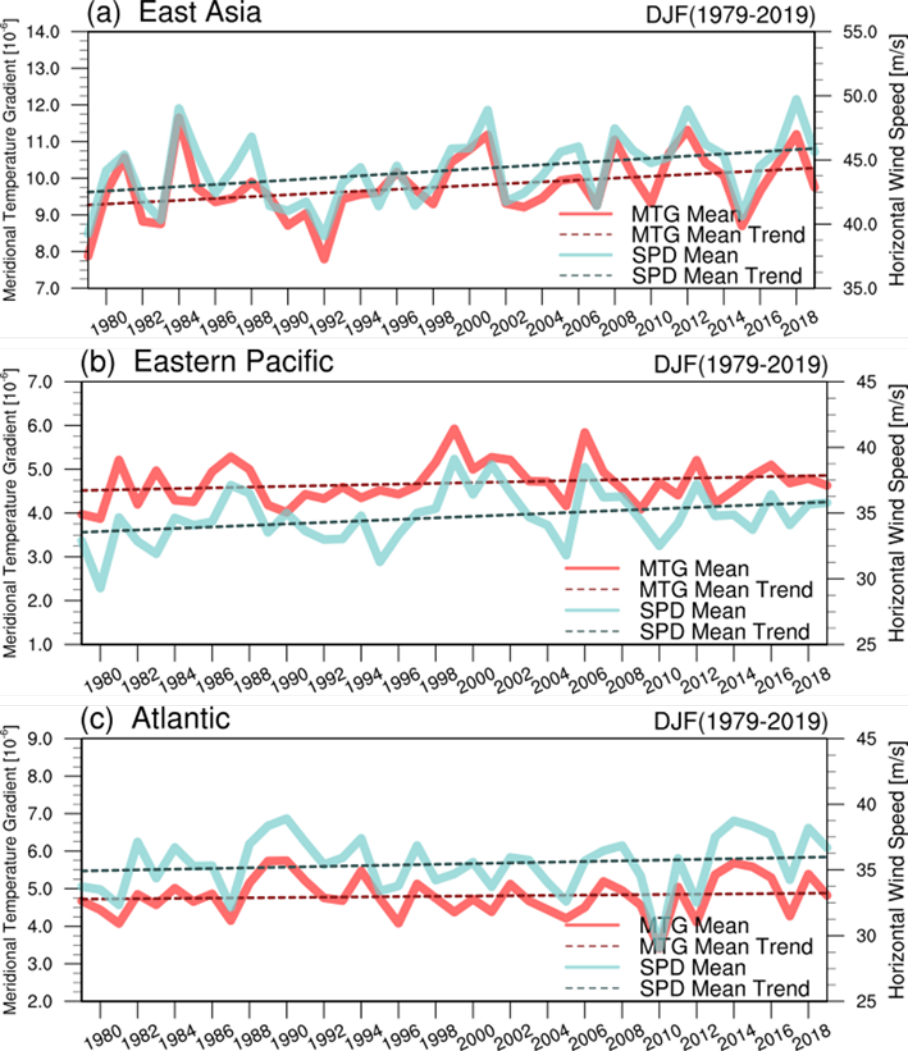


Figure13.

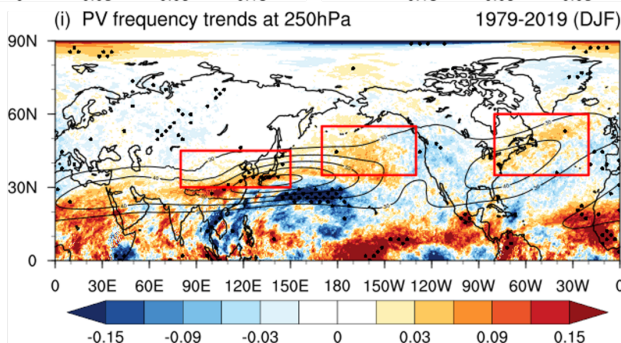
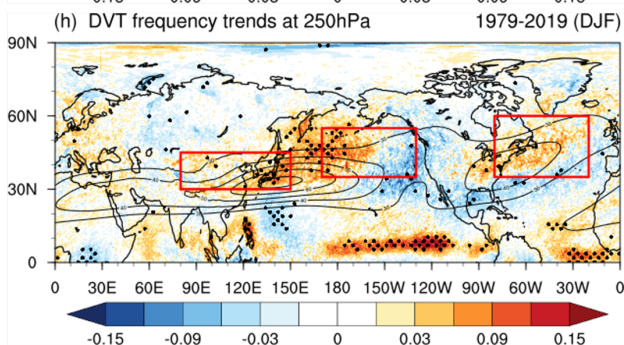
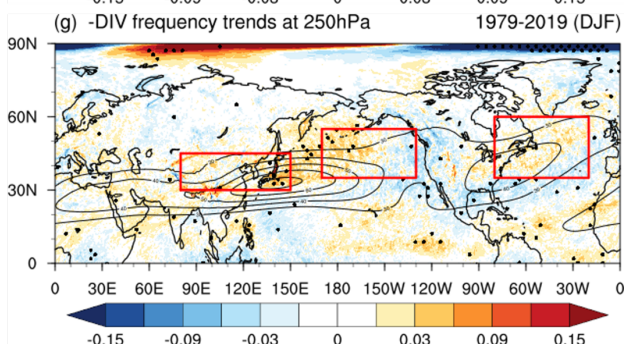
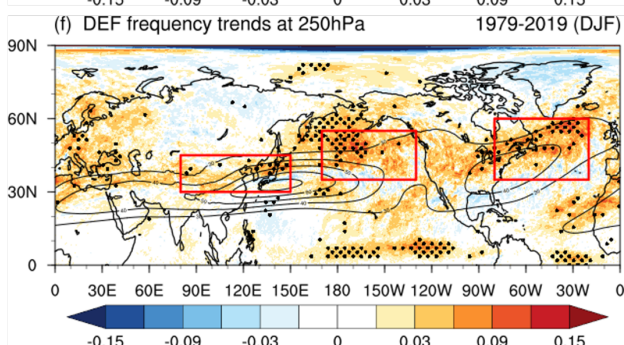
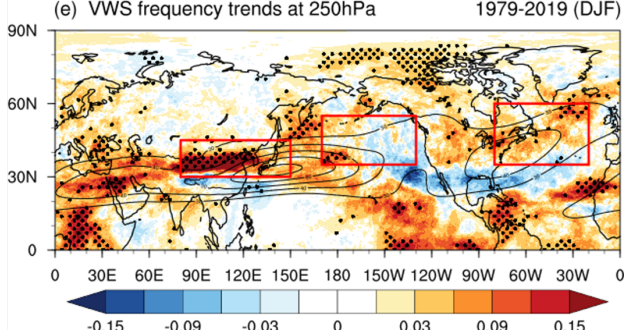
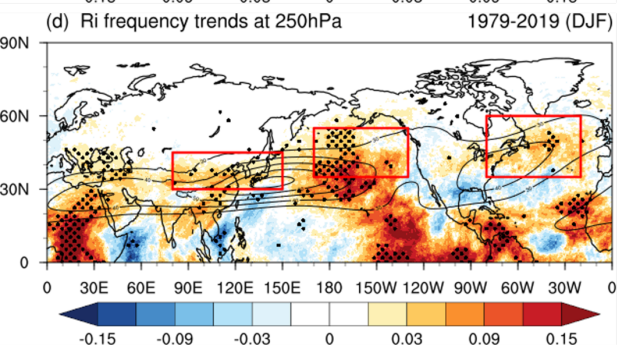
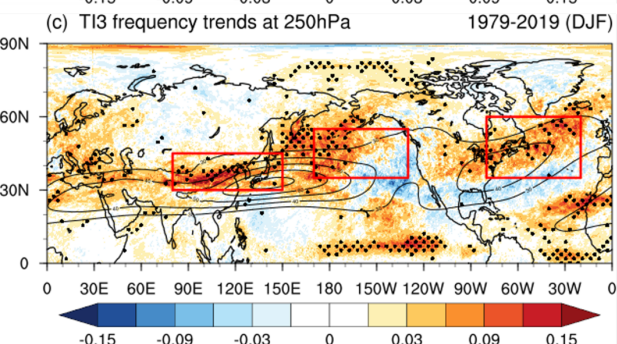
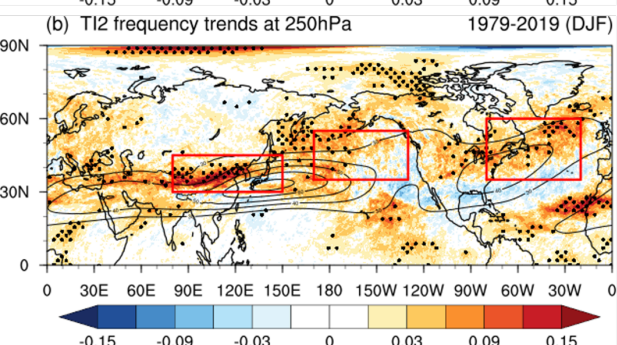
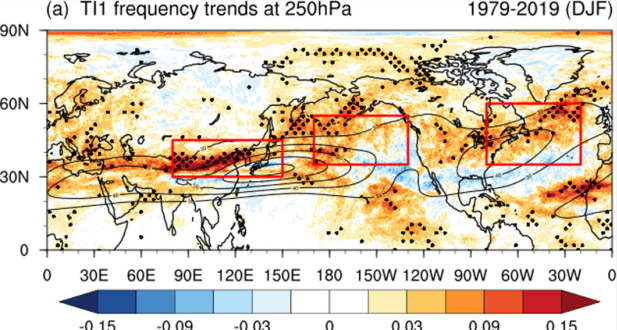
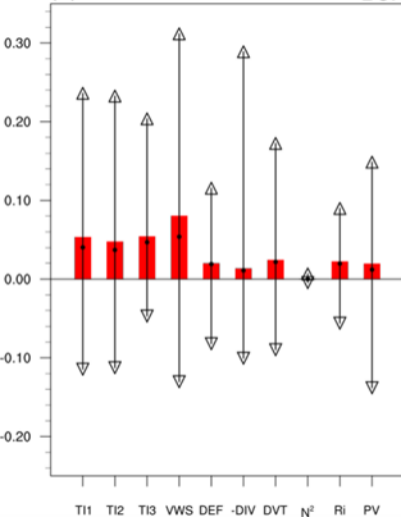


Figure14.

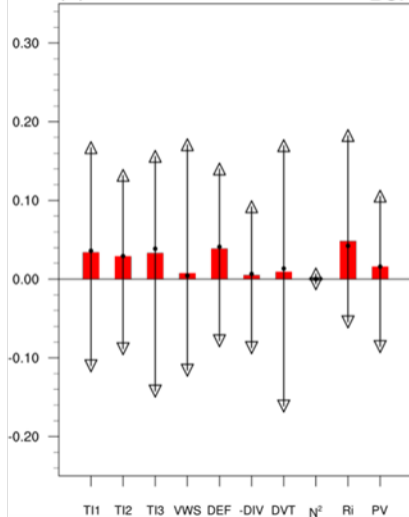
(a) East Asia

DJF



(b) Eastern Pacific

DJF



(c) Atlantic

DJF

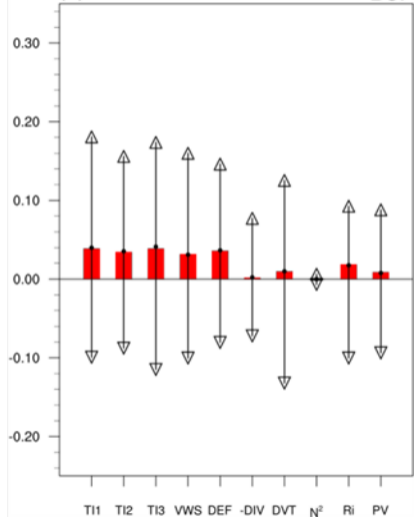


Figure15.

EDR density (2016.01-2021.09)

